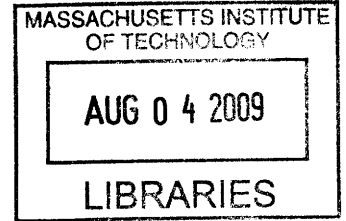# Temperature Dependence of Impurity Resonances in Cuprate Superconductors

by

Kamalesh Chatterjee

Submitted to the Department of Physics
in partial fulfillment of the requirements for the degree of

Doctor of Philosophy

ARCHIVES

at the

MASSACHUSETTS INSTITUTE OF TECHNOLOGY

June 2009

Author ....
Department of Physics
March 09, 2009

Certified by ....
Eric W. Hudson
Associate Professor
Thesis Supervisor

Accepted by ....
Thomas J. Greytak
Professor, Associate Department Head for Education

Temperature Dependence of Impurity Resonances in Cuprate Superconductors

by

Kamalesh Chatterjee

Submitted to the Department of Physics
on March 09, 2009 in partial fulfillment of the
requirements for the degree of Doctor of Philosophy in
Physics

ABSTRACT

In conventional superconductors the superconducting gap in the electronic excitation spectrum prevents scattering of low energy electrons. In high temperature superconductors (HTS) an additional gap, the pseudogap, develops well above the superconducting transition temperature T_C. The identity of this pseudogap and its relationship to high temperature superconductivity is one of the most interesting outstanding problems in condensed matter physics today.

In this thesis I present a new avenue of investigating the pseudogap state, using scanning tunneling microscopy (STM) of resonances generated by single atom scatterers. First, I report that impurity resonance peaks, near zero bias in the excitation spectrum, continue to exist above the superconducting transition temperature and prove that the impurity resonance peak is unchanged through the superconducting transition. I also show that native impurity resonances coexist spatially with the superconducting gap at low temperatures. These findings demonstrate that properties of impurity resonances in HTS are not determined by the nature of the superconducting state, as previously suggested, but instead provide new insights into the pseudogap state. I will further provide preliminary results of doping dependence as a probe to study the pseudogap.

In addition to these scientific results, I will also discuss advances I have made in STM instrumentation, from a novel technology to provide the excitation for the coarse approach mechanism of the STM to current amplifier circuits for faster spectroscopy measurements.

Contents

4

Chapter 1

Conventional and high temperature superconductivity

Macroscopically, superconductivity is manifested by a collection of material properties, the two most important of which are zero resistance (Onnes 1911) and perfect diamagnetism (Meissner effect) (Meissner 1933). As the material is cooled through a temperature called the transition temperature, T_C, the resistance suddenly drops to perfect zero; the material is perfectly conducting, hence the name "superconductor". It was also found the material expels all magnetic fields below the transition temperature.

Besides zero resistance and perfect diamagnetism, many other properties of the superconducting state are also important. The properties are numerous, instead of giving a historical and exhaustive account I only mention a couple to discuss gap in the excitation spectrum. It was found that the transition temperature depends on the average atomic mass (Maxwell 1950, Reynolds 1950) indicating the role of lattice vibrations. Temperature dependence of the specific heat of Sn below the transition temperature is of

the form $ae^{-b/T}$ (Goodman 1953). This implies a special superconducting ground state where a gap opens up in the electronic excitation spectrum.

1.1 BCS theory of conventional superconductivity

In conventional superconductors, an attractive electron-electron coupling develops as a result of interaction between electrons and the atomic lattice. In the language of modern solid state physics, the attractive electron-electron interaction is mediated by phonons. This effective attractive interaction between two electrons due to electron-phonon

5

coupling is at the heart of conventional superconductivity in metals and alloys. The first electron couples with the lattice and polarizes it and the second electron interacts with the already polarized lattice. Cooper (1956) demonstrated that the interaction (however small) makes the Fermi sea of a normal metal unstable. In the weak coupling limit we have (Grosso 2000)

$$U_0 n_0 (E_F) << 1 \quad leading \quad to \quad \Delta_b << \hbar \omega_D \tag{1.1}$$

$$\Delta_b = 2 \hbar \omega_D e^{-2/U_0 n_0 (E_F)} \tag{1.2}$$

The wavefunction of electrons are singlet s-wave Cooper pairs.

BCS Hamiltonian (Bardeen 1957) is given by

$$H_{BCS} = \sum_k (\hbar^2 k^2 / 2m - \mu)(c_{k\uparrow}^+ c_{k\uparrow} + c_{-k\downarrow}^+ c_{-k\downarrow}) + \sum_{kk'} U_{kk'} c_{k\uparrow}^+ c_{-k\downarrow}^+ c_{-k'\downarrow} c_{k'\uparrow} \tag{1.3}$$

Variational determination of the ground state wavefunction is done by minimizing the quantity $W_S = \langle \Psi_S | H_{BCS} | \psi_S \rangle$, where the ground state wavefunction is given by $|\psi_S\rangle = \prod_k (u_k + v_k c_{k\uparrow}^+ c_{-k\downarrow}^+)|0\rangle$ with appropriate constraints on u_k and v_k.

At sufficiently low temperatures, Cooper pair formation can occur without being frustrated by thermal excitations. Each pair can be considered a bound state of two electrons with opposite spin and momentum. The superconducting ground state results from the condensation of these Cooper pairs into a single macroscopic quantum state, making it one of the few examples of a quantum state occupying familiar, non-microscopic length scales and having directly observable effects.

1.2 Gap in the density of states

The macroscopic quantum wave function associated with the BCS ground state typically has s-wave symmetry, equivalent in all momentum space directions. The formation of Cooper pairs opens an energy gap (width Δ) in the density of electronic states at the Fermi energy. This gap Δ is proportional to the pairing energy in the formation of Cooper pairs. Within the gap, no quantum states exist for the unpaired electron. At energies $E >$ Δ (outside the gap), new excited states called Bogoliubov quasiparticles appear. Near the Fermi energy, these quasiparticles have a density of states (DOS) and dispersion relation very different from electrons in the parent metallic state.

$$N_s(E) = \frac{E}{\sqrt{E^2 - \Delta^2}} \quad for \quad E \geq \Delta$$

$$= 0 \quad for \quad E < \Delta$$

(1.4)

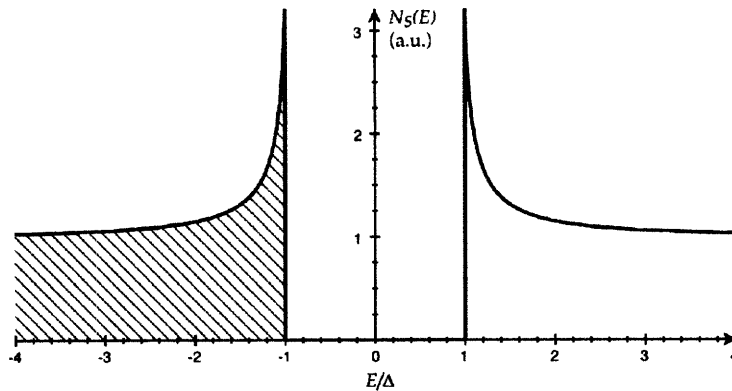The density of states is plotted in Fig. 1.1

Figure 1.1   Theoretical density of states of an s-wave BCS superconductor, filled states are shaded (Slezak 2007).

7

1.3 Discovery of high temperature superconductivity

The BCS theory explains all the experimental observations of "conventional superconductivity" in metals and alloys. Typical transition temperatures are low, for example 4.15 K in Hg, 3.72 K in Sn and 23.3 K in Nb_3Ge. With the objective of increasing transition temperatures, "high temperature superconductivity" was discovered in 1986 and it continues to be a major field of study in condensed matter physics. Though these transition temperatures are still much below room temperature, the name "high temperature superconductors" was coined to reflect the excitement of the initial discovery of transition temperatures forbidden by BCS theory (Bednorz 1986). Initially high temperature superconductivity was found in layered copper oxide materials. Recently Iron pnictide compounds (Kamihara 2008) are found to possess unusual superconducting properties as well. This thesis limits its scope to layered copper oxide materials.

Bednorz and Muller discovered in 1986 that $La_{2-x}Ba_xCuO_{4+\delta}$ has a superconducting phase with a record-breaking transition temperature T_C near 29 K (Bednorz 1986). Soon it was followed by $T_C = 95$ K $YB_2Cu_3O_{6+x}$ (Wu 1987) and Tl doped $HgBa_2Ca_2Cu_3O_{8+\delta}$ (Sun 1994) with a transition temperature of 138 K. The basic building block of all cuprate high-temperature superconductors is a perovskite structure with quasi-two-dimensional CuO_2 sheets as shown in Fig. 1.2. Electronic coupling perpendicular to the copper-oxide plane is very weak. In the La_2CuO_4 family of materials, doping is achieved by substituting Sr or Ba ions for La atoms. This results in holes in the copper oxide plane. In other families of cuprates the mechanism of doping relative to the parent compound is slightly different, but all materials share the feature of weakly coupled CuO_2 planes.

1.4 $Bi_2Sr_2CaCuO_{8+\delta}$ Crystal structure

Superconductivity at the high temperature of 95 K was first reported in $Bi_2Sr_2CaCuO_{8+\delta}$ by Maeda *et al.* in January 1988, a result which was rapidly reproduced by others. The system's crystal structure was reported by Subramanian *et al.* (1988), and it is now known to belong to a class of layered superconductors, denoted Bi-22(n-1)n, which have n=1, 2 or 3 CuO_2 layers per half unit cell (Maeda 1996, pp. 8-10). The most common of these crystal structures and the most widely studied, Bi-2212 (or BSCCO), has a structural diagram which is presented in Fig. 1.2. The structure is pseudo-tetragonal, based on an A-centered orthorhombic subcell. The **a** and **b** axes refer to axes at 45° to the Cu-O bond direction, as shown. With this notation, $\mathbf{a} \sim \mathbf{b} \sim 5.4$ Å.
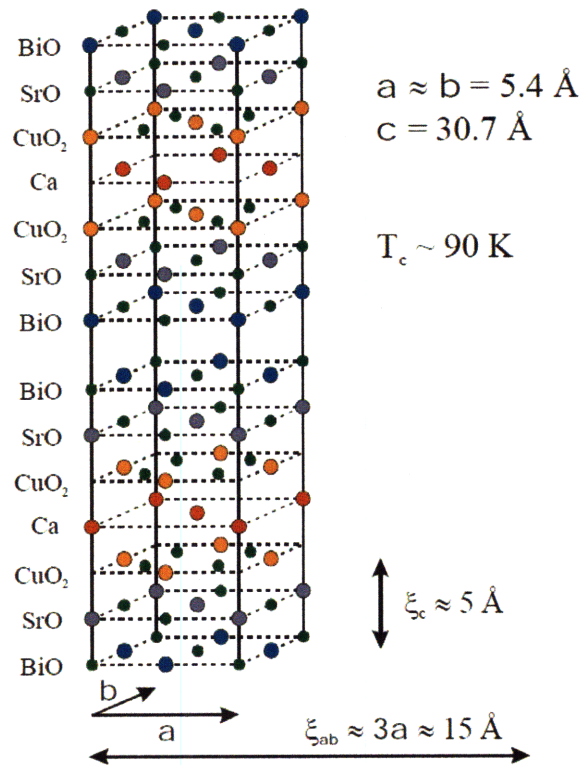

Figure 1.2   Schematic of a single unit cell of $Bi_2Sr_2CaCuO_{8+\delta}$ In each layer the oxygen is represented by the smaller circles. (Hudson 1999)

9

The actual crystal structure is more complicated due to the existence of an incommensurate supermodulation, running throughout the bulk BSCCO crystal. This "superlattice," whose wave vector q ~ $\mathbf{b}*/4.732$, was first observed by Subramanian et al. (1988), is now widely believed to originate due to the presence of additional O atoms in the BiO plane, which lead to a buckling of each of the atomic layers, displacing atoms from their ideal orthorhombic lattice sites along all three crystal axes.

These additional O atoms are also responsible for doping holes into the CuO_2 plane. To first order, each O atom might be assumed to capture two electrons leading to a hole content $p = 2x$, where x is the number of additional O atoms in the system. However, studies have shown that O atoms contribute fewer holes that this, the exact number is unclear due to the difficulties of producing an otherwise stoichiometric sample and of counting the number of additional doped O atoms.

1.5 Doping a Mott insulator – the phase diagram

All cuprate parent compounds have copper oxide planes with occupancy of one electron per unit cell. At this electron concentration the plane is a "Mott insulator," the parent state from which high-T_C superconductors are derived. A Mott insulator is a material in which the conductivity vanishes as temperature tends to zero, even though band theory would predict it to be metallic. Examples of Mott insulators include NiO, $LaTiO_3$, and V_2O_3 (Imada 1998). However, the high-T_C cuprates are the only Mott insulators known to become superconducting when the electron concentration is changed from one per cell.

In a conventional band insulator conductivity is blocked by the Pauli Exclusion Principle. If the highest occupied band contains two electrons per unit cell, electrons have no place to move due to filled orbitals. In the case of Mott insulator conduction is blocked instead by electron-electron repulsion. Copper is doubly ionized and is in a d^9 configuration. It's d shell has a single hole per unit cell. According to band theory, the band is half-filled and must be metallic. However, there is a strong repulsive energy cost of putting two holes (or electrons) on the same ion. This energy, commonly called U, dominates over

the hopping energy t; the ground state is an insulator due to strong correlation effects. It also follows that the Mott insulator should be antiferromagnetic because when neighboring spins are oppositely aligned energy gain by virtual hopping is $4t^2/U$. This is called the exchange energy J. If the amount of charge per cell is fixed, only the electron spin on each site can fluctuate. Virtual charge fluctuations in a Mott insulator generate a "super-exchange" (Anderson 1959) interaction, which favors antiparallel alignment of neighboring spins. This antiferromagnetic Mott insulator is shown in the left side schematic of Fig. 1.3, as described in the simplified single band picture of Zhang and Rice (Zhang 1988a). Coulomb repulsion prevents electron hopping from Cu to Cu, and the exchange correlation is antiferromagnetic in sign.
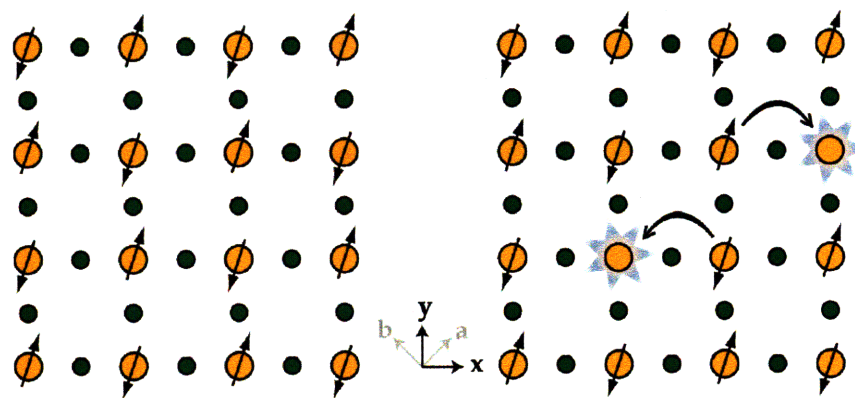
Figure 1.3   Simple schematic of CuO_2 plane. Bond axes (x/y) and BSCCO crystallographic axes (a/b) are shown. Left - square lattice with one spin-1/2 state at every vertex. Coulomb repulsion prevents electron hopping in an antiferromagnetic ground state. Right - 15% hole doping, electron hopping becomes possible (Orange = Cu, green = O). Figure – (Slezak 2007)

Doping these insulating CuO_2 layers with holes (or electrons) causes the appearance of new electronic ordered states, including high-temperature superconductivity. This is because with doping, hopping of electrons from Cu to Cu becomes possible—as shown in the right panel of the figure.

As the antiferromagnetic insulator is doped with holes the antiferromagnetic order is quickly suppressed and is removed at 3-5% hole concentration. The material enters a superconducting phase with increased doping. In the phase diagram of Fig. 1.4 the plot of

11

the transition temperature is dome shaped with a parabolic dependence on doping. As the doping is increased T_C increases but above some doping of approximately 15% T_C drops with increased doping and superconductivity completely disappears as the doping is increased above ~28%. The region of the phase diagram below the doping corresponding to maximum T_C is called "underdoped" region and above it is called "overdoped" region.
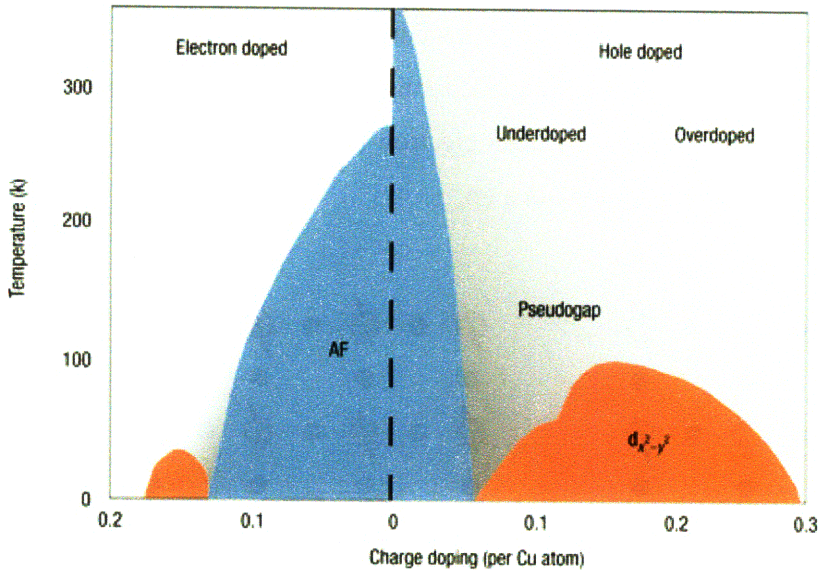
Fig. 1.4　　　　A typical cuprate phase diagram (Bonn, 2006)

Cuprates in general can also be doped with excess electrons in the copper-oxide plane as shown on the left side of phase diagram of Fig. 1.4. On the electron-doped side the antiferromagnetism is robust and survives till doping ~14%. However, superconductivity is present for a narrow range of doping and the transition temperature is significantly low compared to the hole doped side. Carriers are more prone to be localized on the electron-doped side so that electron doping is closer to dilution by nonmagnetic ions, which is less effective in suppressing antiferromagnetic order than itinerant carriers. Another possibility is that the next-neighbor hopping term favors the antiferromagnet on the electron-doped side (Singh 2002). This thesis is limited to the study and discussion of materials in the hole doped side.

For hole-doped materials, in the underdoped region immediately above the transition temperature is called the "pseudogap" region and has many unusual properties. The region on the overdoped side is better understood and many of its features are understood by Fermi liquid theory. However, the region above optimal doping has some strange properties as well, though different from the pseudogap region. This region is called the "strange metal" or "non-Fermi liquid" regime.

1.6 Highlights of experiments

Because of the unusual normal and superconducting state properties and richness of the possible phases, the cuprates have been studied by numerous experimental techniques. It is impossible to give a complete review of the important experiments. In this section I do not follow a chronological order nor claim an exhaustive list but only discuss a few experiments to highlight important properties of cuprates. As a proof of $d_{x^2-y^2}$ pairing, for example, I refer only to the scanning SQUID microscopy result; however, this has been confirmed by many others. For a complete discussion on experiments I refer to some excellent reviews, ARPES (Damascelli 2003), STM (Fischer 2007), Impurities and NMR (Alloul 2007), optical measurements (Basov 2005). Only the experiments presenting a direct proof of a fundamental question like pairing etc. are summarized below.

In conventional superconductors electrons pair into spin singlet states (s = 0, l = 0) and condense into a macroscopic wavefunction with strong overlap in real space (Bardeen 1957). The superconducting state arises due to the instability of the Fermi surface resulting from a weak attractive interaction coming from electron-phonon coupling. In my view, one of the most important experimental results proved that high-T_C superconductivity involves pairing of two electrons as well. Magnetic flux trapped in cylinders is quantized by ħ/2e, (Gough 1987) (ħ is Planck's constant and e is the charge of an electron). Magnetic vortices in bulk samples are also quantized in units of ħ/2e (Gammel 1996). Direct imaging of these quantized bundles of magnetic flux also became possible with new scanning magnetic microscopy techniques. Scanning Hall microscopy measurements (Wynn 2001) imaged individual vortices in bulk single crystals, and

scanning SQUID microscopy measured quantized flux (Bonn 2001) trapped in micrometer-scale rings.

The next topic is about the underlying interaction responsible for pairing. If it is phonon mediated as in BCS theory or some sort of electron-electron interaction? The difference between the dynamics of the normal and superconducting state is striking. Many different experiments, microwave conductivity (Bonn 1992), thermal conductivity (Krishana 1995), infrared conductivity (Puchkov 1996) and photoemission (Kaminski 2000) determined that the scattering rate of the electrons at low energies drops highly as the temperature is lowered in the superconducting state. Mean free path for electrons are very short in the normal state of YBCO but of the order of microns at low temperature. Electron–phonon mediated superconductors are expected to retain strong inelastic scattering even at low temperatures, since phonons are not gapped in the superconducting state. This provides strong evidence for an electron-electron interaction as the origin of pairing.

The next important question that could be answered experimentally is whether the pairing state is a spin singlet as in s-wave BCS or spin triplet and the symmetry of the pairing state. NMR measurements of the Knight shift demonstrated that spin susceptibility decreases rapidly below T_C, thus eliminating the possibility of a spin-triplet state (Takigawa 1989, Barret 1990). This forces a symmetrical orbital wavefunction, either the $l = 0$ s-wave state or some higher angular momentum such as $l = 2$ (d-wave).

Many experiments were performed to determine the exact paring symmetry. The temperature dependence of the London penetration depth is linear, favoring a d-wave density of states (Hardy 1993). The energy gap mapped out by ARPES has nodes that lie in the [110] direction (Shen 1993), 45° from the copper-oxide lattice vectors, indicating a possible $d_{x^2-y^2}$ state. A more definitive answer was found with scanning SQUID microscopy of a superconducting ring formed around this axis where three crystal orientations are fused together. In a $d_{x^2-y^2}$ state, the phase change in this tri-crystal

geometry leads to supercurrent and a half-superconducting flux quantum (1/2 of $\hbar/2e$) in the ring, a result confirmed by Tsuei *et al* (Tsuei 1994).

The pseudogap regime has numerous properties that can not be explained by Fermi-liquid theory, the standard theory of weakly interacting electrons. Here I shall quote just a few I consider most important or puzzling. The d.c. electrical resistivity changes linearly with temperature as opposed to the expected T^2 dependence when the source of resistance is scattering of electrons from one another (Batlogg 1994). Muon spin relaxation (μSR) measurements find local order on short length scales far into the superconducting regime, indicating the presence of magnetism (Niedermayer 1998), a result also pointed to by Kerr effect (Kapitulnik 2008) and neutron scattering (Fauque 2006).

Cuprate high-temperature superconductors exhibit many important differences from conventional superconductors. One of the striking differences between cuprate and conventional superconductors is in their characteristic length scales. In high temperature superconductors these scales are near 1 nm: the Cu interatomic distance $a_0 \sim 0.3$ nm, the interdopant atom distance $L \sim 1.5$ nm, the Fermi wavelength $\lambda_F \sim 1$ nm, and the superconducting coherence length $\lambda \sim 1.5$ nm. This means that different electronic phenomena, which are usually at dramatically different spatial scales in a metal, can interact strongly with each other at the nanoscale in cuprates. No widely accepted pairing mechanism has been identified to explain superconductivity in the cuprates.

1.7   A typical d –wave density of states

Experiments have definitively shown that the superconducting state possesses $d_{x^2-y^2}$ symmetry. Figure 1.5 illustrates the momentum dependence of the energy gap.
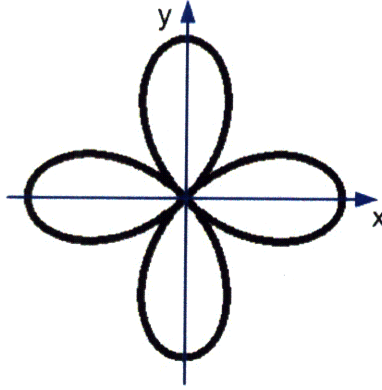
Figure 1.5 $d_{x^2-y^2}$ symmetry of the gap magnitude in momentum space.

It has nodes (i.e. takes zero values) in directions called "nodal directions," 45° to the crystal axis. In the bismuth-strontium-calcium cuprate family of superconductors, these directions align with the *a/b*-axes of the crystal (Fig. 1.2). The antinodes, directions in which the gap reaches its maximum value Δ_0, coincide with the *x* and *y*-directions, defined by the square lattice formed by the copper atoms. The density of states relation eq. 1.4 is modified reflecting the direction-dependence of the gap. The density of states will also be direction dependent and integration over all directions gives the total density of states.

$$N_s(E) = \int_0^{2\pi} \frac{E}{\sqrt{E^2 - (\Delta_0 \cos 2\theta)^2}} d\theta \tag{1.5}$$

The expected density of states for a d-wave superconductor is plotted in Fig. 1.6.
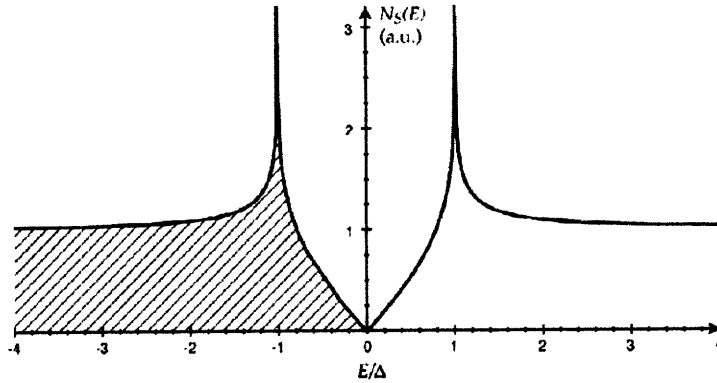
Figure 1.6   Theoretical density of states for a BCS superconductor with d-wave gap symmetry (Slezak 2007).

1.8   Single layer cuprate Bi₂Sr₂CuO₆₊δ

In this thesis I report results from the single layer compound $Bi_2Sr_2CuO_{6+\delta}$ (Bi-2201). Many of its properties are similar to the more widely studied $Bi_2Sr_2CaCuO_{8+\delta}$ (Bi-2212). This section provides the detailed crystal structure (Fig. 1.7) and quotes related literature for reference. Bi-2212 was studied widely and the results of Bi-2201 we study here can now be compared and contrasted. Bi-2201 also allows access to the highly overdoped region of the phase diagram, which is not accessible to Bi-2212 (Takeuchi 2001). Thus our studies allow new insights into the cuprate phase diagram. The transition temperatures for Bi-2201 are considerably lower ($T_{C\ Max}$ = 35 K for our optimally doped samples) than those in Bi-2212 ($T_{C\ Max}$ = 95 K). So it becomes relatively easy to track atomically resolved region of sample as it passes through transition temperature from low temperature. In addition, at lower temperature thermal broadening is less significant and extracting information from STM data is easier. The STM is also more stable at lower temperatures.

17
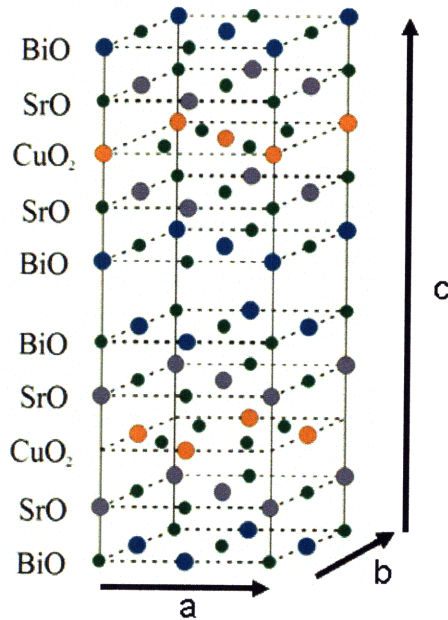
Figure 1.7   The unit cell for $Bi_2Sr_2CuO_{6+\delta}$ is similar to that of other cuprates. The structural parameters for the unit cell of $Bi_2Sr_2CuO_{6+\delta}$ are a ~ b = 5.4 Å and c = 24.4 Å (Rajagopal 1993).

The main result of this thesis is based on studies of 15 K overdoped $Bi_{2-y}Pb_ySr_2CuO_{6+\delta}$ where y = 0.38 (Kondo 2005). Pb is added to the samples supplanting Bi atoms to remove the supermodulation which is intrinsic to the non-Pb-doped crystals (Takeuchi 2001). Removing the supermodulation is not important to our studies, but is important for experimentalists using scattering techniques. Aside from removing the supermodulation, Pb-doping also leads to a modest increase in T_C (Rajagopal 1993). The underdoped and optimally-doped crystals used in this thesis are also doped with La which allows access to those regimes by acting as a type of "charge reservoir" (Kondo 2005, Okada 2006).

Chapter 2

STM operation and instrumentation

After the introduction to high temperature superconductivity in the last chapter, here I present the theory and instrumentation of the Scanning Tunneling Microscope (STM). All the studies on superconducting samples described in this thesis are done with a custom built Scanning Tunneling Microscope (STM). In the first section I describe tunneling theory and show how the important measurements, topography and spectroscopy, are done. Next, I describe the experimental set up and list important aspects of the STM head that enable us to track individual atoms as temperature is increased. In the last section I provide a systematic study of different amplifiers circuits we tested as our current amplifier.

2.1   Theory of Scanning Tunneling Microscopy

A scanning tunneling microscope consists simply of a sharp tip (a piece of wire), which is brought within several Angstroms of a sample surface, and moved with respect to that surface. The tip and sample, both electrical conductors, have a bias voltage applied between them, which results in a measurable current tunneling through the vacuum that separates them.   The current signal is amplified and recorded. The tunneling current depends on the bias voltage, separation between the tip and the sample, the local density of states and the tunneling matrix element. Although detailed models of imaging and spectroscopy with an STM are necessarily complex, I will present only a very straightforward theory of tunneling, first proposed by Bardeen (1960) and applied to

STM by Tersoff (1983, 1985) soon after the invention of scanning tunneling microscopy (Binnig 1982a & 1982b).
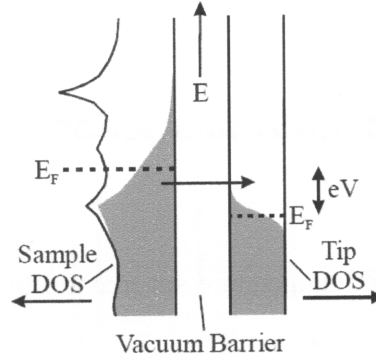
Figure 2.1   Schematic of tunneling from sample to tip. The Fermi energies of the sample and tip, are separated by an energy eV due to the application of a sample bias voltage *V*. This allows electrons to tunnel elastically through the vacuum barrier, resulting in a measurable current. The magnitude of this current depends on the density of states of both tip and sample, on the distance between them, on the voltage applied, and on the amount of thermal broadening (as pictured here by the shaded filled states, obtained by multiplying the density of states by the Fermi function) (Hudson 1999).

The tip and sample are treated as two separate systems whose wave functions slightly overlap. Perturbation theory can then be used to determine the rate of electron transfer between the systems. Assuming energy conservation in the tunneling process (elastic tunneling), the current is given by

$$I = I_{sample \rightarrow tip} - I_{tip \rightarrow sample}$$
$$= \frac{4\pi e}{\hbar} \int_{-\infty}^{\infty} |M|^2 \rho_s(x, y, E_s) \rho_t(E_t) \left(f(E_s)[1 - f(E_t)] - f(E_t)[1 - f(E_s)] \right) d\varepsilon \quad (2.1)$$

where e is the electron charge, $\hbar$ is Planck's constant over 2π, $|M|$ is the tunneling matrix element, and ρ is the local density of states for either the sample (s) or the tip (t). The Fermi function, f(E), is defined as

$$f(E) = \frac{1}{1 + \exp\left(\dfrac{E - E_f}{k_B T}\right)} \qquad (2.2)$$

in which E_f is the Fermi energy, k_B is Boltzmann constant, and T is temperature.

An intuitive way to understand eq. 2.1 is outlined below. For each electron in the sample at energy ε, there is some chance that that electron will tunnel to the tip, thus creating an electron current from the sample to the tip. The probability of tunneling depends on the number of states that the electron could tunnel to, i.e. the number of empty states available at energy ε in the tip multiplied by the number of full sample-states (number of electrons that could tunnel). The number of full sample-states is given by the product of the sample density of states with the Fermi function, both evaluated at energy ε. The umber of empty states is found by subtracting the Fermi function from unity. This gives the first term in the equation. To obtain the net total current from the sample to the tip, the reverse current from the tip to the sample is subtracted and the results are integrated over all energies. A schematic of tunneling is provided in Fig. 2.1.

For elastic tunneling E_s and E_t are separated by the bias voltage V. Defining all the energies with respect to Fermi energy, eq. 2.1 may be rewritten

$$I = \frac{4\pi e}{\hbar} \int_{-\infty}^{\infty} |M|^2 \rho_s(x, y, \varepsilon - eV) \rho_t(\varepsilon) [\mathrm{f}(\varepsilon - eV) - \mathrm{f}(\varepsilon)] \, d\varepsilon \qquad (2.3)$$

2.1.1 Dependence of matrix element with tip-sample separation

Although the derivation of the matrix element M will not be discussed here, I provide a qualitative explanation based on elementary quantum mechanics. An electron in the sample encounters a step-like potential barrier between itself and the tip. The electron's chances of getting through the barrier depend on the value of its wave function once it reaches the tip. However, from simple quantum mechanics of a particle at a step we

know that the sample-electron wave function is decaying exponentially inside the barrier. Thus, the chance that the electron will tunnel diminishes exponentially with the width of the barrier (tip-sample separation). Or in other words, the current depends exponentially on the separation between the tip and the sample. A simple explanation of this dependence can be found in the excellent book by Chen (p. 3 Chen 1993).

The dependence of tunneling matrix element with tip-sample separation is given by

$$|M|^2 \propto \exp\left(-2\frac{\sqrt{2m\varphi}}{\hbar}s\right) \approx \exp\left(-\sqrt{\varphi(\text{eV})}\ s(\text{Å})\right) \qquad (2.4)$$

in the approximation that $V \ll \varphi$, where φ is the convoluted work function of the tip and sample and m is the electron mass. A further assumption that the tunneling matrix is independent of energy (at least for small energies) leads to the simple dependence

$$I = I_0 \exp\left(-\frac{s}{s_0}\right) \qquad (2.5)$$

In the next sections I shall describe how the above equations are used to make topographic and spectroscopic maps of the sample surface.

2.1.2 Topographic imaging with STM

One common mode of operation for a scanning tunneling microscope is that of constant current topography. Figure 2.2 presents a block diagram of the feedback loop used to keep a constant current flow as the tip is scanned back and forth across the sample. The feedback loop changes and records the scanner voltage in order to keep the tunneling current constant for every location. The strong exponential dependence of tunneling current implies very small change of the tip-sample separation s to keep the current constant so that the tip is at a constant distance from the sample surface. As the work function is typically on the order of 4 eV, an increase in tip-sample separation of only 1 Å can decrease the current by a factor of $e^2 \sim 7.4$. Due to this strong dependence, measurement of variations in the scanner voltage as a function of lateral position serve as

high resolution topographic images of the surface. The high spatial resolution of the image is the consequence of atomically sharp tip.
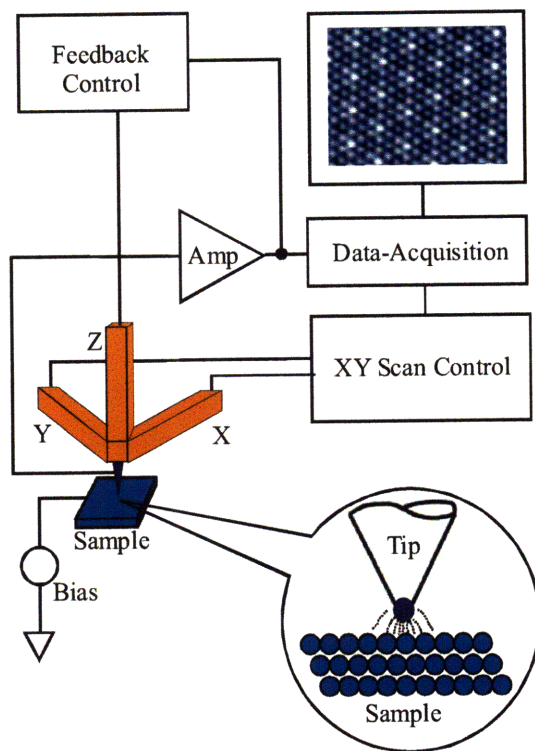
Figure 2.2   Schematic of operation of a scanning tunneling microscope. An atomically sharp tip is brought within a few Angstroms of an atomically flat surface. Feedback maintains the tip/sample separation by holding the tunneling current constant (Hudson 1999).

2.1.3 Differential conductance spectroscopy

STM can measure the local density of states directly. The first demonstration of this measurement, referred to as scanning tunneling spectroscopy (STS), was by Stroscio (1986) on Si(100). Assuming small sample bias (V), the tunneling matrix element may be considered a constant with respect to energy and removed from the integral yielding

$$I \propto \frac{4\pi e}{\hbar} \int_{-\infty}^{\infty} \rho_s(x,y,\varepsilon-eV)\rho_t(\varepsilon) \left[f(\varepsilon-eV)-f(\varepsilon)\right] d\varepsilon \tag{2.6}$$

The density of states for tip is usually constant for in the energy range of interest. If the temperature is low enough to approximate the Fermi function as a step function, $\theta(\varepsilon)$.

$$I \propto \int_{-\infty}^{\infty} \rho_s(x,y,\varepsilon-eV) \left[\theta(\varepsilon-eV)-\theta(\varepsilon)\right] d\varepsilon$$

$$I \propto \int_0^{eV} \rho_s(x,y,\varepsilon-eV) \ d\varepsilon \tag{2.7}$$

Differentiating the above equation

$$\frac{dI}{dV}(x,y,s,V) \propto \rho_s(x,y,eV) \tag{2.8}$$

Thus a measurement of the differential tunneling conductance, dI/dV, yields a quantity proportional to the local density of states. The factor that relates dI/dV to ρ_s is a function of, among other things, the tip-sample separation, s. The explicit form of the dependence of this factor on s can be obtained from an examination of the equation for the tunneling matrix element. Using this equation, we can write

$$\frac{dI}{dV}(x,y,s,V) = A\exp\left(-\frac{s}{s_0}\right)\rho_s(x,y,eV) \tag{2.9}$$

where A does not depend on s.

We typically measure the differential tunneling conductance by setting the tip-sample separation, characterized by the junction resistance at a given sample bias, and then turning off feedback so that this separation is fixed. A small, sinusoidal voltage modulation is then applied to the bias voltage, and the resulting current modulation, as read by a lock-in amplifier attached to the output of the current amplifier, is proportional to the differential conductance. This can be seen using the Taylor expansion of the current

$$I(V+dV\sin(\omega t)) \approx I(V) + \left.\frac{dI}{dV}\right|_V \cdot dV\sin(\omega t) \tag{2.10}$$

The AC component of the current can be read directly using a lock-in amplifier and is proportional to the differential conductance (dI/dV) and hence to the LDOS. This measurement is repeated for different bias voltage resulting in LDOS "spectra" as a function of energy.

2.1.4 Differential conductance mapping

A natural extension of the above technique is to measure lateral position dependence as well as energy dependence. In this case, rather than measuring the conductance at a single position, it is measured at all the points on the surface defined by a close grid. At a given spatial position, the differential conductance at one or more energies is measured. Then, the tip is moved, using feedback as in topography mode, to the next position, at which point the feedback is once again disabled and the differential conductance measurements are made. This mapping technique allows easy visualization of the evolution of the DOS with position. Such a data set is often will be referred to as a *spectral-survey or conductance map*. Spectral-surveys can provide a wealth of information, and much of the data contained in this thesis is derived from them.

2.2 Description of the experimental set up

All the data presented here are taken with a custom built Scanning Tunneling Microscope (STM). I outline a few salient points about the complete experimental set up. This description is not exhaustive; the complete description will appear in a forthcoming RSI publication from our group and a thesis by Doug Wise. Scientifically, we wanted to study changes in material properties as the material passes through the transition temperature T_C. For this we need a variable temperature STM that can track atomically resolved regions from a low temperature (2-4K) to temperatures above 150K. This temperature range is enough to study the high temperature superconductors through T_C. We have the required cryogenic set up involving a liquid helium dewar found in previous low temperature STM set ups. Low temperature STM has advantages over room temperature

STM including high spectroscopic resolution, low pressure due to cryo-pumping, reduced thermal drift, and stability of the surfaces under observation. The samples are cleaved in situ (in vacuum) and since STM studies the sample surface good vacuum is required to prevent surface contamination. We operate at temperatures from low (4 K) to room temperatures, so ultrahigh vacuum (UHV) is essential. In order to achieve UHV we have the required pumps and a vacuum chamber with appropriate flanges for connections to the external world and manipulators to handle samples as well as to control thermal connection and vibration isolation. Vibration isolation is done in two stages; a granite table is suspended from air springs, the experiment hangs from the table, however, a second in-vacuum isolation stage was found to be necessary. The in-vacuum vibration isolation also provides thermal isolation. The most unique feature in the set up is cryogenic sample storage area; this allows us to clean the tip frequently (when required) and quickly by applying high voltage between the tip and a gold sample.

2.3   Description of the STM head

Most previous variable temperature STM designs are unable to track individual atoms over temperature changes; thermal expansion of the microscope moves the tip-sample junction far away from its original location after warming or cooling. Our STM head is built with a high degree of symmetry and with materials chosen such that the thermal expansion of the various components of the STM largely cancels out. Macor was chosen for most of the body of the microscope because of its high stiffness and low thermal contraction. All electrical wires leading to the microscope are made of copper and are thermally connected to the variable temperature stage so that all parts of the STM are at a uniform temperature.

The main components in the STM head are indicated in Fig. 2.3. The scanner is the most important part which responds to the electrical signals and produces motion in the atomic scale; it has a range of only 200 – 300 nm. To bring the STM tip within the scanner range a coarse approach mechanism is required. We use "walker" consisting of six shear piezo stacks (1) which act on a triangular sapphire prism (2) to which the tip is attached. The design has been described elsewhere in detail (Pan 1999). The position of the tip (3) is

measured by a capacitive position sensor. A metallized cylinder of Macor (4) with inner diameter 0.60 inch is attached to the bottom of the sapphire prism. Concentric to this is a cylinder of copper (5) with outer diameter 0.57", which is fixed to the body of the microscope. As the tip holder moves, the overlap between these two cylinders changes, resulting in a change in their mutual capacitance. The change in capacitance due to even a single walker step (100 nm) can easily be detected by a commercial capacitance bridge; we use the Andeen-Hagerling 2550A. Because we know the approximate position of the sample, we can rapidly move the tip to a point very close to the sample before beginning a careful final approach, greatly reducing turnaround time.
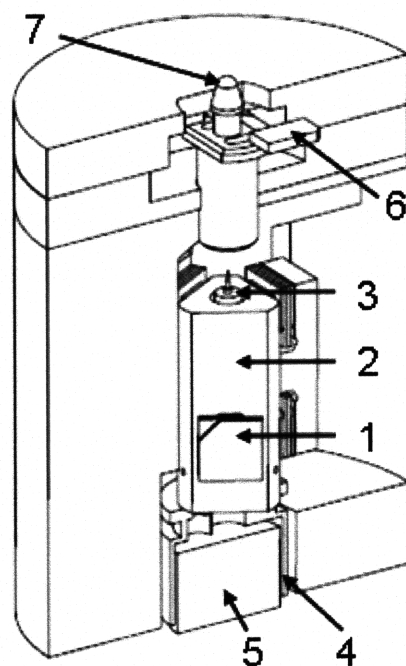
Figure 2.3   Cross section of our STM (actual size). Piezo stacks (1) move a sapphire prism (2) onto which the tip (3) is mounted. The position sensor works by measuring capacitive overlap between a cylinder (4) attached to the tip, and a stationary cylinder (5). Conducting pads (6) allow electrical contact to the sample mount (7).

Samples are mounted at the top of the STM. We use a spring-loaded sample holder. Four gold-plated molybdenum pads (6) are epoxied onto an anodized aluminum cylinder.

These pads provide electrical contact to the sample. The sample is placed on a stud (7) which bridges the gaps between these pads, and is held firmly in place by a stainless steel conical spring (not shown), which can exert significant force while occupying very little space. A cryogenic thermometer and UHV-compatible resistive heater are mounted on this assembly. The entire sample holder is made of highly thermally conductive materials, ensuring uniformity of temperature throughout the experiment.

2.4   Control electronics

The STM control electronics was purchased from Topometrix Inc. A DSP based feedback control system operates at 100 kHz, with three 16 bit ADC's (one continuously monitors the current from our current amplifier, and two others are used for additional inputs, such as output from our lock-in amplifier), five 16 bit scan DAC's with high voltage amplifiers (which supply between ± 220 V to drive the tube scanner), and a 16 bit DAC which provides ± 10 V for sample bias. The system also comes equipped with additional inputs to allow the addition of voltage modulations to both the bias (used for dI/dV measurements) and Z-piezo outputs, as well as with multiple digital IO ports, one of which is used to trigger our walker controller.

The system required some modification of both the electronics interface and the software. The software modifications were done by Eric Hudson (Hudson 1999) and documented in his thesis. In order to improve noise performance the I/O board has been removed from the electronic controller and the grounding is reorganized, individual filters housed in separate metal enclosures are assembled inside the controller enclosure and multipin connectors at the rear panel of the controller has been replaced with BNC connectors. Frequency selectable filters for the scanner signals have been installed, which we usually set at 3 kHz, but could be low as 10 Hz for highly sensitive spectroscopic measurements. Additionally, we insert a divider (by 10 or by 100) into the sample bias line (which increases the energy resolution to approximately 30 mV or 3 mV respectively).

2.5 Current amplifier

The primary task of STM is to measure currents; the most important instrument in determining the system performance is the current amplifier. This section discusses different amplifier circuits we tested. Before delving into the circuit topology we provide an order of magnitude calculation of the maximum possible theoretical bandwidth based on the current we measure. The constraint of maximum theoretical bandwidth arises due to the discreteness of electrons. Typical currents to be measured are 100 pA at a bias voltage 100 mV, however, it is required to measure small signals around the set point value, typical bias modulation is 1 mV, so we need to measure currents ~1 pA. A high resolution spectral survey often takes days and the data acquisition time is directly dependent on the bandwidth, hence the bandwidth is very important.

Let us assume a bandwidth of 10 kHz, we would then see if we can improve upon it. Time interval available to count the number of electrons = 0.1 ms. Number of electrons in 0.1 ms

$$N = \frac{10^{-12}}{1.6021 \times 10^{-19}} 10^{-4} \approx 625 \tag{2.11}$$

Signal to noise ratio $= \sqrt{N} = 25$

For signal to noise ratio of 25 the bandwidth is 10 kHz if we want to measure 1 pA ac signal. However, for signal to noise ratio of 10, the bandwidth is 62.5 kHz.

A commercially available current amplifier 1212, manufactured by Ithaco and distributed by D.L. Instruments has the benefits of variable gain (10^4 to 10^9 V/A) and overvoltage and overcurrent protection. It has good precision and a bandwidth of 3 kHz for a gain setting of 10^9 V/A (1 mV/pA). We designed a well isolated linear power supply to power the amplifier. It is well isolated to eliminate ground loop problems and a linear power supply rather than switched mode to have less power supply noise. The actual bandwidth available is much less due to many non idealities, around 1.5 kHz; hence we tried amplifier designs based on different commercially available integrated circuits.

29

2.5.1 Two stage amplification

The DL1212 uses discrete FETs. We have tried using available ICs for our application and designed three circuits based on these ICs; AD549, OPA 627 and OPA 128. The important components of the circuit are presented in Fig. 2.4. The gain is distributed between two stages. It is usually difficult to stabilize a circuit with two stage gain; however, we successfully operated the circuit with good stability margins with appropriate choice of compensation elements and a low pass filter between the two stages. The first stage is the precision current to voltage converter using the current amplifier IC (AD549 or OPA 627 or OPA 128 as the case may be) the second stage could be any precision FET amplifier and we used OPA 227 in our circuit. The circuit using OPA 627 resulted in the best bandwidth of about 4 kHz for the same overall gain of 10^9 V/A. Noise at the output is about the same 4 mVpp (equivalent to 4 pApp). The amplifiers designed in the lab are mounted directly to the vacuum feedthru on top of the cryostat.

Two stage amplification is better for this very low current measurement because the main resistance R_{high} is usually very high and its associate parasitic capacitance can not be avoided. A lower value of resistance would usually have much better dynamic performance due to lower parasitic resistance. By reducing the gain of the first stage a lower value of R_{high} could be used.

2.5.2 Extracting the ac part

High amplifier bandwidth is required during data acquisition in spectroscopy mode where the lock-in measures the change in current corresponding to a small change in voltage. The lock-in takes the total current as input and extracts the signal corresponding to the set frequency. In our design using a high pass filter we extract the ac signal at the amplifier and provide it as an additional output. This enables us to provide more gain (times 100) to the ac signal. The high pass filter consists of R_2 and C_2. The amplifier A_3 as indicated in Fig. 2.4 provides the high gain to the ac signal. For the same bandwidth it improves the

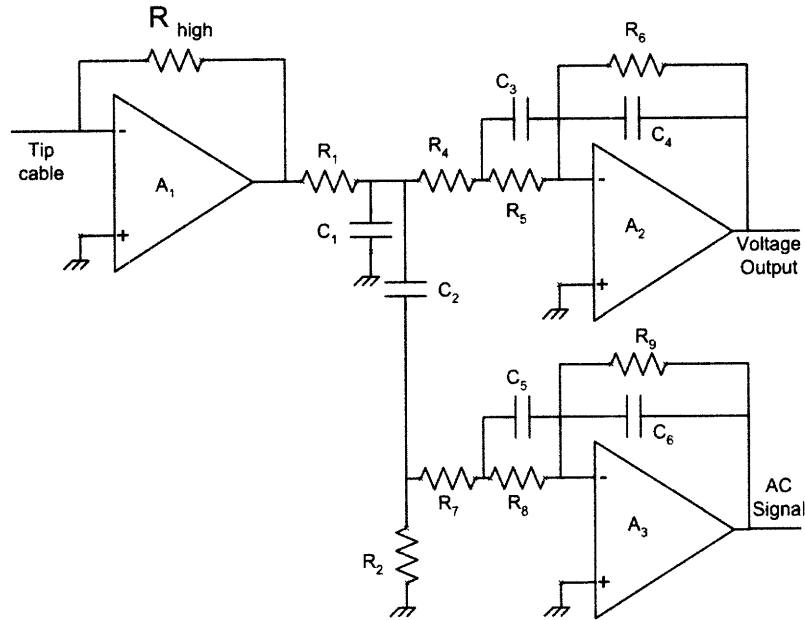signal to noise ratio for the ac signal. We consider this a major improvement over existing amplifiers.

Figure 2.4   Schematic of the circuit for two stage amplification (A_1 &A_2) and extraction of the ac signal (A_3). R_1 and C_1 constitute a first order low pass filter required to reduce high frequency interaction between the two stages. R_2 and C_2 is high pass filter for ac extraction. R_4, R_5, R_6 not only set the gain of the second stage but in combination with C_4 and C_3 determine the lead lag compensation parameters.

2.5.3 Composite amplifier

Single or multistage classical FET based Op amps in circuit configurations similar to Fig. 2.4 have excellent performance in applications where the required gain bandwidth is low compared to the gain-bandwidth product of the op amp. As the closed loop gain increases the error reducing loop gain decreases and can eventually produce significant errors at higher frequencies. Current-feedback op amps or other high bandwidth op amps have good dynamic performance at both low and high gains. In a current feedback amplifier the feedback components set both closed-loop gain and open-loop gain, making loop gain and dynamic performance relatively independent of closed-loop gain. Unfortunately, the

dc performances like output and input offset voltages, common mode rejection and noises of current feedback amplifiers are poor compared to classical op amps.

A composite amplifier using a classical amplifier and the OPA603 current-feedback amplifier or other higher speed amplifier can combine the best qualities of both amplifiers. Figure 2.5 gives a simplified schematic of the inverting composite amplifier. The components required at different gains for a current feedback amplifier could be found in the data sheet and guidelines for component selection are discussed in Kalthoff (1991). The overall amplifier has the dc performance features of OPA 627, for example very low input offset current and input offset voltage. Since the input stage does not drive the load directly the dc accuracy can be better than the single stage classical amplifier.
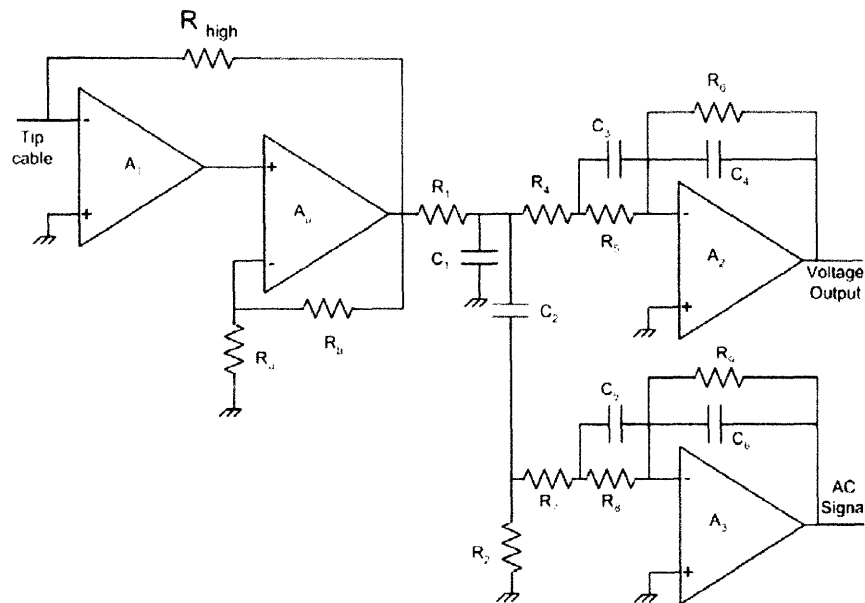

Figure 2.5   Schematic of the composite amplifier. The second amplifier in the composite stage is indicated as A_μ. The second stage of signal amplification A_2 and the ac signal extraction circuit with A_3 is similar to Fig. 2.4.

The current to voltage gain of the composite amplifier is set by R_{high} alone. Errors due to R_a and R_b do not affect the gain of the composite amplifier. The gain of the second amplifier, set by R_a and R_b, should be within ±5% to assure expected dynamic performance. Slew rate and full-power response of the classical amplifier are boosted in the composite amplifier. In out tests we got a slightly improved bandwidth of 5 kHz compared to 4 kHz with the classical amplifier. The parasitic resistance in parallel to R_{high} is connected to the output of the second amplifier in the composite amplifier configuration and this results in improved performance as well.

Composite amplifiers are difficult to stabilize; the stability depends on the set point current; this is undesirable despite some small increase in bandwidth. Based on these studies the recommendation is to use classical amplifiers with second stage of gain 10 and gain 100 for the ac stage. Extracting the ac signal is a successful new technique to improve signal to noise ratio for the same bandwidth and should be incorporated as part of routine data acquisition.

Chapter 3

Drive circuit for coarse approach motion

In the last chapter I described the need for a coarse approach mechanism in order to bring the tip from a macroscopic distance (say 1 mm) to within the scanner motion range (200 – 300 nm) without crushing the sample. This coarse approach is achieved by a "walker" which in our design makes use of shear piezos. Shear piezoelectric motors frequently require large voltage changes on very short time scale. Since piezos behave electrically as capacitors, this requires a drive circuit capable of quickly sourcing or sinking a large amount of current at high voltages. Here we describe a novel circuit design using a high voltage amplifier, MOSFET switching stage and auxiliary capacitor. This circuit can drive the piezoelectric motors at much higher speed, lower cost, and better flexibility for computer automation than conventional methods. We illustrate its application in a controller for a scanning tunneling microscope coarse approach mechanism, where it is capable of switching 4.7 nF PZT-8 shear piezoelectrics through 400 V in 0.5 µS at a repetition rate of 10 kHz, delivering a peak current of 20 A. We also discuss other possible applications and modifications of this circuit.

Piezoelectric motors, capable of nanoscale precision over millimeter ranges of motion, have come into common usage, particularly in the coarse approach mechanism of scanning probe microscopes. Although a number of different designs exist, many share a common set of motions – a slow ramp, in which the piezo stays firmly attached to the object being moved, and a rapid slip, in which the piezo breaks frictional contact with the object and slides along it. Driving this rapid slip can prove challenging, as the piezo, which electrically behaves as a capacitor, needs to be charged or discharged through

34

hundreds of volts in microsecond time scales, requiring the driver to source or sink high transient currents. Unfortunately, the high voltage amplifiers commonly used for driving piezoelectric devices rarely have both the high internal slew rate and high transient output current necessary to provide such charging and discharging currents.

Here we describe a straight-forward and novel solution to this problem: the introduction of an auxiliary capacitor at the output of the amplifier to supply high transient currents and of a switching MOSFET stage to provide the switching speed. We have used this idea to design and build a piezo controller for the course approach mechanism ("walker") for our scanning tunneling microscope (STM) to illustrate one possible use of this circuit. We begin section 3.1 by describing the shear piezoelectric STM walker and section 3.2 by outlining the requirements of a controller to drive this walker. We then describe the circuit design in section 3.3, presenting both a block diagram of the circuit as well as required waveforms. Finally, in section 3.4 we provide a comparison with other typical drive methods and describe the advantages of this scheme.

3.1 Mechanical description of the walker

A variety of coarse approach mechanisms have been designed for scanning probe microscopes, initially mechanical (Fein 1987, Sonnenfeld 1987, Demuth 1986, Kaiser 1987) and more recently using piezoelectric motors (Pohl 1987, Renner 1990, Frohn 1989, Guha 2003, Agrait 1992, MacLeod 2003, Gupta 2001, Blackford 1997, Rust 1997, Chen 1994). We have chosen to use the Pan design (Pan 1999) because of its stability and reproducibility of motion. Although this STM coarse approach mechanism has been described elsewhere (Pan 1999), we provide an overview of the Pan-type walker here to highlight the drive requirements. As shown schematically in Fig. 3.1 and as a photo in Fig. 3.2, a triangular sapphire prism (MarkeTech) housing the STM scanner is supported by six supports (feet), with three aligned near the top and three near the bottom of the prism. Multiple piezos in a stack increase the shear distance (about 100 nm for 400 V applied at 4 K). Each foot consists of a stack of four shear piezos (Staveley), topped by a ceramic pad (CoorsTek) which is in direct contact with the sapphire prism. The force

35

between the feet and the prism, which is held by friction, is maintained by an adjustable spring plate on one side.
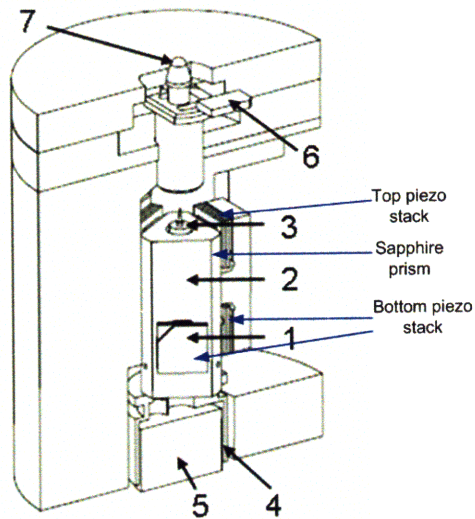
Figure 3.1   Mechanical arrangement of the walker. Similar to Fig. 2.3, description of components 1 - 7 are same. The Piezo stacks (same as 1) and the prism (same as 2) are highlighted. There are six piezo stacks, three top and bottom sets, each 120 degrees apart.

Figure 3.2   Photograph of top part of the prism and walker stacks. Two top piezo stacks are indicated; the third one on the front is pulled apart and not shown in this picture. The bottom piezo stacks are not shown in this photo as well. Sapphire prism is also indicated.

This setup enables precision motion as shown schematically in Fig. 3.3. The piezo stacks ("feet") are glued to the macor body (cross-hatch) but free to s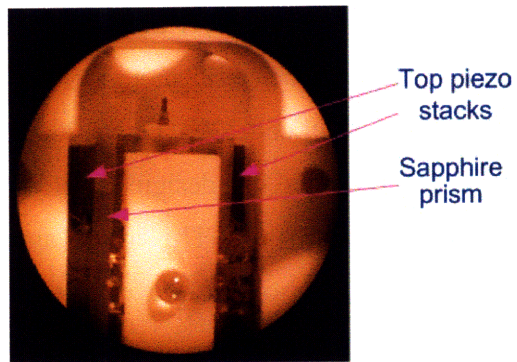lip along the sapphire prism when rapidly excited. A step begins with all piezos discharged. Each foot is then driven in turn, slipping along the sapphire prism, which is held fixed by the friction of the other feet. After all feet have been sheared (Fig. 3.3b) they are simultaneously and slowly discharged, pushing the sapphire prism to a new equilibrium position (Fig. 3.3c) to complete the step. The sequence portrayed in Fig. 3.3 is for a forward step. Backward motion may be obtained by either reversing the polarity of the drive or, better to prevent any small incidental forward motion during a backward step, by time reversing the process.
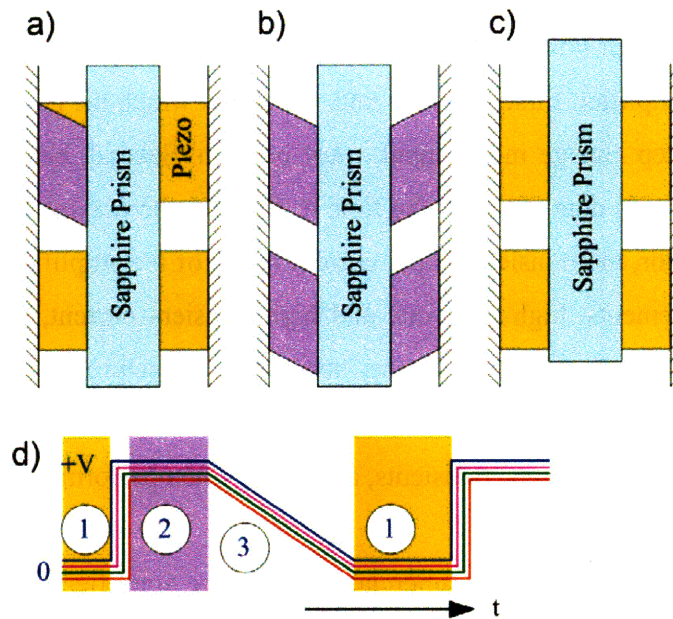

Figure 3.3   (a,b,c) Schematic of one step movement in forward direction and (d) the waveforms we use to drive this motion. Starting from an uncharged position (d1), each foot is individually slipped backward while the others hold the prism still (a). Once they have all slipped (b, d2) they are slowly ramped back (d3) to their rest position, pushing the prism forward (c).

37

3.2 Limitations of conventional circuits

The waveform we use to drive this motion is shown schematically in Fig. 3.3d, where each curve represents the voltage applied to one piezo stack, vertically offset for clarity. The most demanding part of the drive is the rapid charging of the piezos needed to force a quick slipping motion without disturbing the prism. A large voltage (we use 400 V for ~100 nm steps at 4 K) must be slewed on the order of a microsecond in order to achieve quick and sizable slip motion.

Electrically a piezo is equivalent to a capacitor, so the rapid excitation process corresponds to a fast charging rate (or, for the time reversed waveform, a fast discharging rate). A common driver circuit generates a waveform in a low voltage circuit and then amplifies it using high voltage amplifier. Fast charging places two often contradictory demands on the amplifier. First, it's slew rate, the rate at which the no load output voltage changes after a step change in the input, must be high. Second, because for capacitive loads charging time is dominated by the time it takes for the maximum output current to charge the capacitor, the transient output current rating of the amplifier needs to be high. These two requirements, high slew rate and high transient current, are unmet by most available high voltage amplifiers. Worse, because manufacturers' amplifier datasheets specify output current for the case of steady output voltage, not the far lower output current available during voltage transients, amplifiers often perform below expectations.

Because of the inadequacies of commercial high voltage amplifiers for driving piezos in this fashion, discrete component amplifiers have been designed (Colclough 2000). However, amplifiers by definition are optimized for best performance when constituent transistors are operating in the linear region; their switching performance tends to be poor.

Another commonly used method for driving piezos is the triac-based circuit. Triacs can deliver very high transient currents and have a reasonably fast switching speed. However, they lack the flexibility of the amplified waveform approach, as they are typically tied to

the 60 Hz sinusoidal utility voltage waveform and thus lack straight forward frequency and amplitude modification.
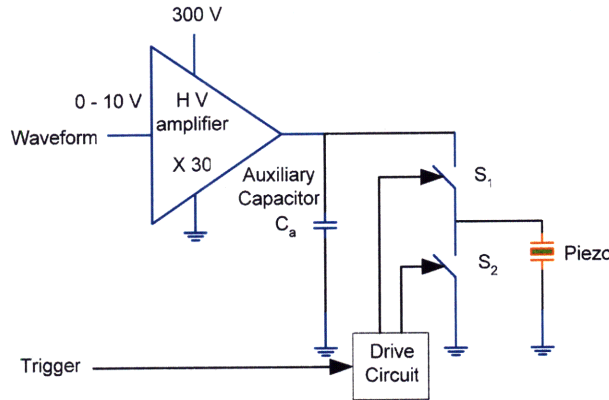

Figure 3.4   Block diagram of the driver circuit. The MOSFETS S_1 and S_2 are indicated as ON/OFF switches. The auxiliary capacitor C_a is at the output of the H. V. amplifier.

3.3   The new auxiliary capacitor based circuit

To overcome these problems we have designed and built a new drive circuit for piezoelectric-based walkers which provides unprecedented switching speed and flexibility. The core concept of our circuit, introduction of an auxiliary capacitor at the amplifier output to supply the switching transients, resolves the conflicting requirements of high transient current and high slew rate. This idea could be used in many general purpose piezo drive applications. Below we describe the operation of the circuit in detail as it was implemented for the shear piezo walker controller used in our STM.

We show in Fig. 3.4 a schematic circuit diagram. We generate two inputs, an analog "waveform" and digital "trigger," using a National Instruments NI6731. The "waveform" input is amplified by a high voltage amplifier (PA92 from Apex Microtechnology), which charges an auxiliary capacitor (C_a = 200 nF). Output is controlled by two high voltage power MOSFETs (IRF840s) connected in a half bridge configuration and operated only in a switching mode, thus their representation as simple switches S_1 and S_2. The switches are complimentary, i.e. $S_1 = \overline{S_2}$, so that one of them is always ON but they

39

are never ON simultaneously. When S_1 is ON the piezo is connected to the amplifier output, allowing charge stored in the auxiliary capacitor to quickly transfer to the piezo stacks. When S_2 is ON the piezo is shorted to ground. The MOSFET state is controlled by a high voltage high speed power MOSFET driver with dependent high and low side referenced output channels (IR2111 from International Rectifier), which itself is controlled by the binary "trigger" input.

As will be apparent below, while all the piezos can be driven by a single amplified waveform, charged by a single auxiliary capacitor, because each foot needs to slip independently, the output to each piezo needs to be controlled by its own pair of MOSFET switches and driver. These "drive circuits" are all activated by a single "trigger" input, however each driver's actual switch trigger is delayed by a different length of time.
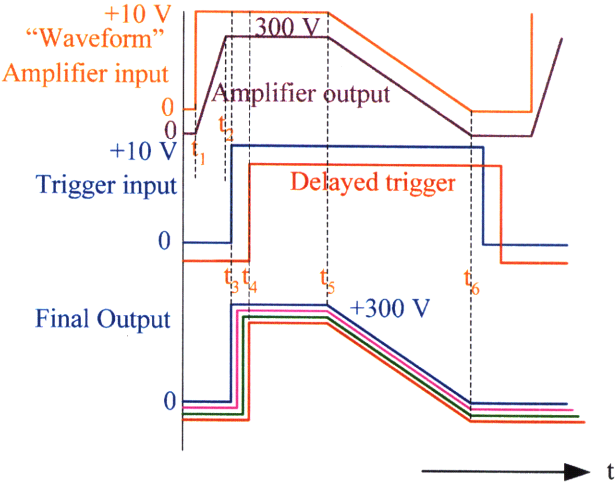

Figure 3.5   Waveforms for forward motion, including the "waveform" input and amplifier output, "trigger" input and one example of a delayed trigger (each foot is driven with a different delay), and the resulting output to each of four feet (of six feet in the real walker), previously described in Fig. 3.3d.

3.3.1 Waveform for driving piezo stacks

Using this combination of a single amplified waveform and a series of time delayed triggers, the piezo walker can be flexibly driven forward or backward. The waveforms for forward motion are depicted in Fig. 3.5. After a step rise at t_1 in the "waveform" input, the amplifier output rises to the required voltage by time t_2. The rise time, $t_2 - t_1 = 20$ μs for our application, is determined by the slew rate and transient output current of the amplifier as well as the auxiliary capacitor. Additional time is provided to ensure voltage stabilization at the desired amplifier output. At this point the amplifier is driving only the auxiliary capacitor – the piezos are grounded through the MOSFET switch.

Turning the "trigger" input high at t_3 results in charging of the first piezo, with current provided by the auxiliary capacitor. The pulsed current rating of a MOSFET is very high (32 A for the IRF840), so the available charging current is essentially limited only by external circuit elements and the wiring resistance. The turn ON time and rise time are about 50 ns for IRF840 MOSFETs, hence the piezo charging appears instantaneous in the time scale of the plot. A series of time delayed triggers between t_3 and t_4 cause the remaining piezos to charge sequentially and stay charged (slipped) until at t_5 the "waveform" input and hence amplifier output ramp down to the rest, uncharged, state. By t_6 the walker has completed one forward step.

Note that because we use a series of time delayed triggers, the turn off times, where those triggers fall to zero and the MOSFETs switch the feet to ground, are staggered by the same amount as the turn on times between t_3 and t_4. Because the amplifier voltage has gone to zero at t_6, this is inconsequential.

For the reverse motion, we use the time reverse of the forward motion, so that the charging process is slow and simultaneous for all the piezo stacks, but the discharging is quick (Fig. 3.6). The step begins with all triggers being set high, turning ON the switch S_1 for all piezos before the amplifier is ramped. To initiate the fast discharge (slipping action), the time delayed triggers fall sequentially, turning switch S_2 ON, and using the
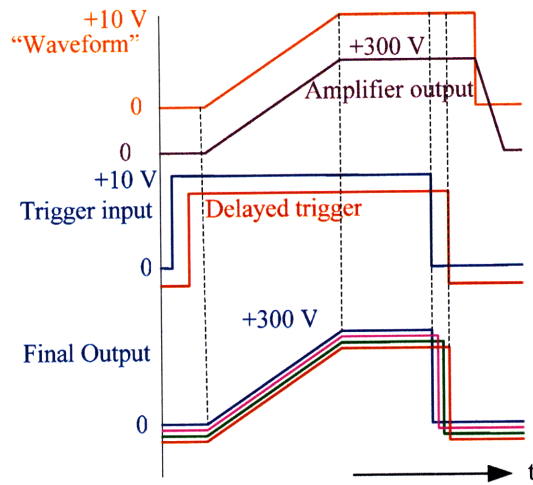
41

Figure 3.6   The waveforms for the reverse motion, simply the time reverse of those in Fig. 3.5.

large current sinking ability of the MOSFETs to pull each foot back to its rest position. Just like the charging current, the discharge current is effectively limited by external components and wiring.

3.3.2   The auxiliary capacitor

The unique ability of this circuit to supply large current during charging comes from the charge stored in the auxiliary capacitor, which has a capacitance value roughly 40 times larger than that of the piezo stacks (we use 200 nF for 4.7 nF piezos). During forward motion, charge from the auxiliary capacitor is quickly transferred to the piezo stacks when the switch S_1 is turned ON. The high transient current does not come from the amplifier. This eases amplifier selection constraints and reduces the cost significantly. The interval between the onset of two consecutive piezo stacks is magnified and presented in Fig. 3.7. The rapid charging of a piezo does result in a small drop of the auxiliary capacitor voltage and hence of all piezos already "turned ON." However, the relatively large capacitance of the auxiliary capacitor ensures that this is a minor effect and has no significant impact on operation. After the drop, the auxiliary capacitor is recharged by an almost constant current from the amplifier. The continuous current rating

of the amplifier thus partially dictates the delay between piezo onsets, as the auxiliary capacitor should charge to full voltage between them.
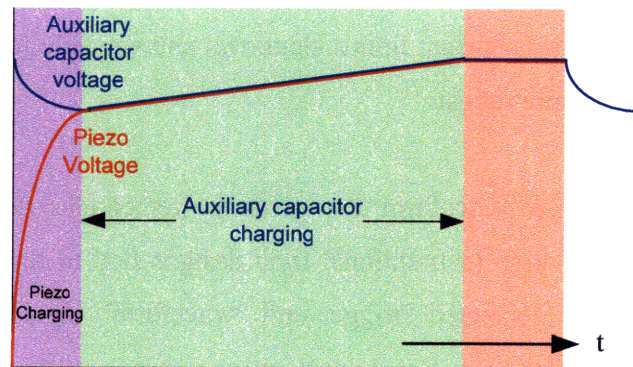

Figure 3.7   Auxiliary capacitor discharging and charging. Zoomed in view of the interval immediately after t_3 in Fig. 3.5. C_a charges the piezo and in the process its voltage drops slightly and then together C_a and piezo get charged to full voltage by the amplifier.

3.4   Advantages of the new auxiliary capacitor based circuit

Compared to previous circuit designs for piezoelectric walkers, our new auxiliary capacitor based design has several important advantages in terms of cost, switching speed, flexibility, and ease of computer interface.

The new circuit is relatively inexpensive, as it shares a single high voltage amplifier for all six drive channels, reducing by a factor of six this most expensive component in the circuit. It is also easy to modify due to its modular nature. Adding more channels, for example, simply requires the addition of a drive circuit, with no additional inputs, while changing the load, for example by driving piezos with higher capacitance, typically requires at most an increase of the auxiliary capacitor. Even a change as large making the circuit bipolar so that voltage levels could swing between positive and negative voltage to generate higher shear displacement, involves modifying the power circuit with four quadrant switches but the control scheme remains the same.

Switching speed in our design is set by the rise time of a single high speed power MOSFET, which is typically faster than the slew rate of amplifiers by orders of magnitude due to their internal composition of many transistors in cascade. Yet by using off-the-shelf amplifiers for the initial waveform amplification we can utilize standard amplifier features such as current limits, shutdown and versatile feedback options, which make the controller more robust.

The use of an amplified waveform also gives us tremendous flexibility and computer control, especially relative to traditional triac designs tied to the 60 Hz utility voltage waveform. Computer generated "trigger and "waveform" inputs allow shaping of the ramp-back, for example to a constant acceleration rather than the constant velocity signal we have depicted here, and also allow frequency control. We typically run at 1 kHz, with no observed reduction in step size from lower step rates, significantly increasing the walking speed.

Beyond its use for a piezoelectric walker, the auxiliary capacitor and MOSFET switching stage concept can be used in a wide range of applications where a good linear amplification is desired along with fast switching transient performance. This technology could be used as a driver for piezoelectric motors in laser modulation, semiconductor growth and etching tools, lithography and micromachining. For applications where the average power output lies within the capabilities of a high voltage amplifier, this design resolves the challenging problem of providing rapid transient currents of tens or even hundreds of Amperes while maintaining waveform flexibility. The capability of driving the walker with any desired waveform further opens up new application possibilities in scientific instruments and nanotechnology.

Chapter 4

Temperature dependence of impurity resonances

After the first introductory chapter about high temperature superconductors and two chapters about instrumentation we are ready to dive into the main scientific result of this thesis – temperature dependence of impurity resonances in Bi-2201 through the transition temperature (Chatterjee 2008). In conventional superconductors the superconducting gap in the electronic excitation spectrum prevents scattering of low energy electrons. In high temperature superconductors (HTS) an additional gap, the pseudogap (Timusk 1999), develops well above the superconducting transition temperature T_C. Here we present a new avenue of investigating the pseudogap state, using scanning tunneling microscopy (STM) of resonances generated by single atom scatterers. Previous studies in the superconducting state of HTS (Balatsky 2006) have led to a fairly consistent picture in which potential scatterers, such as Zn, strongly suppress superconductivity in an atomic scale region, while at the same time generating low energy excitations whose spatial distribution – as imaged by STM (Hudson 2001, Pan 2000) – is indicative of the d-wave nature of the superconducting gap. Surprisingly, we find that similar native impurity resonances coexist spatially with the superconducting gap at low temperatures and survive virtually unchanged upon warming through T_C. These findings demonstrate that properties of impurity resonances in HTS are not determined by the nature of the superconducting state, as previously suggested, but instead provide new insights into the pseudogap state.

In d-wave superconductors, such as the high temperature superconductors (HTS), impurities act as pair breakers, giving rise to virtual bound states, or resonances, within the gap. For strong scatterers these resonances lie close to the Fermi energy, and significantly modify bulk superconducting properties (Maeda 1990, Kluge, 1995). The local (atomic scale) effects of these resonances have been studied by several probes, such as nuclear magnetic resonance (NMR) (Bobroff 2001, MacFarlane 2000, Ouazi 2006, Tallon 1997, Williams 2000) and muon spin relaxation (μSR) (Nachumi, 1996). A variety of scanning tunneling microscopy (STM) studies of impurity resonances in HTS have been reported, including studies of native (unidentified) impurities (Hudson 1999, Hudson 2003), intentionally doped Zn and Ni impurities (Hudson 2001, Pan 2000) and intentionally placed surface impurities (Yazdani, 1999). All of these STM studies demonstrated that impurity resonances are associated with an enhanced local density of states inside the gap, close to the Fermi energy. All of these studies were also performed on $Bi_2Sr_2CaCu_2O_{8+x}$ (Bi-2212) near 4 K, significantly below T_C.

Here we report on temperature-dependent STM studies of native impurities in overdoped ($T_C = 15$ K) $Bi_{2-y}Pb_ySr_2CuO_{6+x}$ (Bi-2201). In addition to allowing comparison to previous studies in Bi-2212, Bi-2201 has the benefit of having a relatively low T_C, thus allowing us to study impurity resonances below and above T_C without the resonance being obscured by thermal broadening.

4.1   Measurement methods and low temperature results

Our measurements are made using mechanically cut Pt-Ir (80%-20%) tips which are cleaned and sharpened through high voltage (800 V) field emission on Au in ultra-high vacuum at low temperatures. Before proceeding to measurements on a sample, we tunnel into Au to verify that the tip has a good work function and a flat density of states between at least ±100 mV, an energy range larger than what is of interest for this study. Samples are cleaved in ultra-high vacuum and at both high and low temperatures resulting in no noticeable topographic or spectroscopic differences with cleave temperature. Although we have observed similar impurity states using multiple samples and tips, for consistency

of temperature dependent results, all scattering resonance data shown in this chapter are taken from a single impurity region.

To perform the temperature dependent measurements discussed here we have constructed an ultra-high vacuum STM with the ability to track atomically resolved regions – here surrounding individual impurities – over a wide range of temperatures. We begin our study at low temperatures, using an experimental methodology similar to that used in previous STM impurity studies (Hudson 2001, Pan 2000). We search for impurity resonances by recording a spectral survey, in which differential conductance spectra (proportional to the local density of states) are recorded on a dense grid over a specified spatial region. In a spectral survey impurity states are easily identified by their enhanced low energy density of states.

After locating an impurity resonance we zoom in and take a high spatial and energy resolution spectral survey to pinpoint the impurity's location, spectral shape, and peak resonance energy. A high resolution topography and simultaneously acquired low energy slice $G(\mathbf{r}, E = -2$ meV) from such a survey are shown in Fig. 4.1. Spectral weight associated with the resonance appears predominantly at the locations of the center and next nearest neighbor Bi atoms, which sit above Cu atoms in the superconducting CuO_2 plane ~5 Å below (Fig. 4.1c).
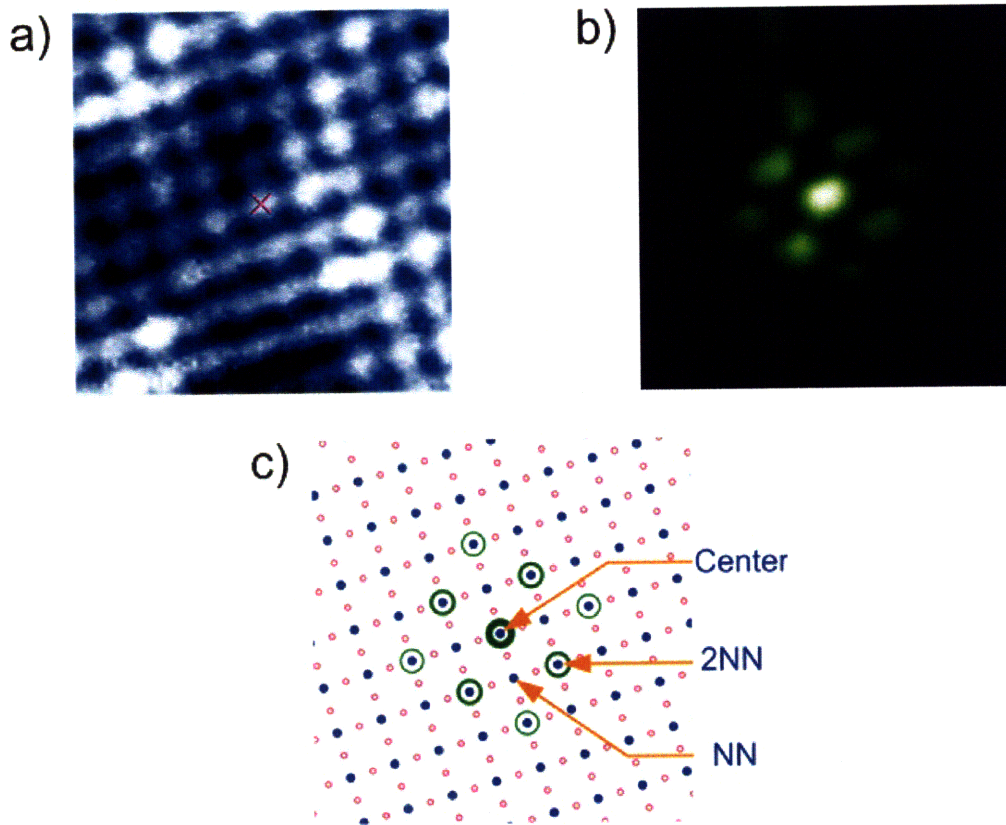
Figure 4.1   Topographic image and spectral map layer around the impurity resonance.
a. 30 Å square topographic image (V_{sample} = -100 meV, I = 400 pA, T = 5.2 K) showing a BiO plane where the Bi and the Pb substituted atoms (brighter) are visible. Pb atoms have no observed associated spectroscopic signatures.
b. Simultaneously acquired differential conductance map corresponding to V_{sample} = -2 meV. The location of the bright center of the impurity resonance is marked by the red "X" on an otherwise indistinguishable Bi atom in the topography of **a.** As Cu atoms in the CuO_2 plane reside directly below the observed atoms, this is consistent with the native impurity being either a Cu vacancy or some element replacing Cu in the CuO_2 plane.
c. Schematic representation of the CuO_2 layer underneath the BiO layer. Blue solid dots represent Cu atoms and pink open circles represent O atoms. The impurity center is shown surrounded by the thickest green circle. The nearest neighbor (NN) Cu atoms correspond to dark regions in conductance map. Next nearest neighbor (2NN) Cu atoms have the second strongest signal in the conductance map.
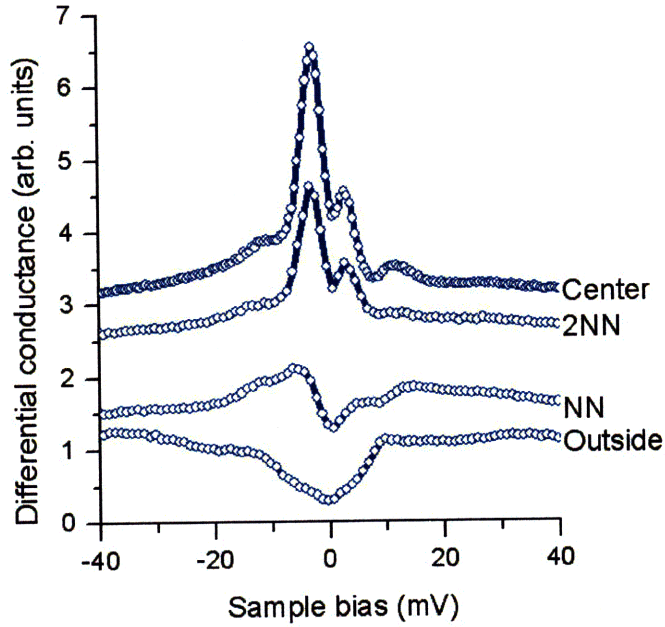
Figure 4.2   Tunneling spectra taken at 5.2 K at different locations within the field of view shown in Fig. 4.1. The spectrum at the impurity center (topmost curve) has a sharp resonance peak at $\Omega = -2.75$ meV. The second peak at symmetric bias ($\Omega^{Sat} = -\Omega = 2.75$ meV) is the "satellite" peak and is likely due to the particle-hole symmetry of Bogoliubov quasiparticles. The spectra on 2NN Cu atoms are similar to those from the center, with a reduction of the main peak amplitude. The spectra on NN Cu atoms indicate the presence of a gap instead of the impurity peaks found on adjacent atoms. A typical spectrum far from the impurity site is shown in the bottom plot. All spectra in this figure and in subsequent ones are taken with the same settings ($V_{sample} = -100$ meV, $I = 400$ pA, $V_{mod, rms} = 780$ μeV) and are vertically offset for clarity.

After identifying the center and shape of the impurity, we place the tip at specific locations and take energy dependent differential conductance spectra. In Fig. 4.2 we show examples of such spectra taken at the resonance center, as well as over nearest neighbor (NN) and next-nearest neighbor (2NN) atoms. Spectra taken immediately outside the resonance show a typical gap structure, here of width $\Delta = 11$ meV. The edge of this gap may also be seen as small peaks in the central and next nearest neighbor spectra. The most obvious feature in these spectra, however, is a low energy peak (centered at $\Omega = -2.75$ meV). It is this peak whose spatial dependence we mapped in Fig. 4.1. In most theoretical treatments of impurity resonances, the energy of this main peak is

49

determined by the strength of the potential scatterer (Balatsky 2006). Following Salkola et al. (Salkola 1996), as has been done in previous analyses of STM results, and considering that the resonance is in a local gap of width $\Delta = 11$ meV, we find that such a peak results from potential scattering with phase shift $\delta_0 = 0.4\pi$ for the resonances reported here, compared to 0.48π for Zn (Pan 2000) and "vacancies" (unidentified native scatterers) (Hudson 2003) and 0.36π for Ni (Hudson 2001). In the unitary (strongest scattering) limit the phase shift would be $\pi/2$. Thus, in this picture, these resonances are generated by strong, although not unitary, potential scattering.

4.2   Temperature dependent measurements

Although the low temperature behavior of these resonances is very similar to those of Zn and vacancies in Bi-2212, our temperature dependent measurements yield surprising results: we find few significant changes in the impurity resonance as we warm through T_C into the pseudogap state. In Fig. 4.3 we show the temperature dependence of spectra from the resonance center. Overlaying the data is the 5.2 K spectrum, thermally broadened to the appropriate temperatures (red lines). Thermal broadening is a purely mathematical procedure – convolution with the derivative of the Fermi function – that accounts for the decreased energy resolution of the STM at higher temperatures. Nearly all features of the higher temperature data are well matched by the thermally broadened low temperature data. This indicates that the resonance is not appreciably affected by temperature, and, in particular, not affected by the transition from the superconducting to the pseudogap state. Similarly, temperature dependent conductance maps (Fig. 4.3b-d) taken at the same location as Fig. 4.1 show a lack of significant spatial change with warming.

From this temperature independence we conclude that, contrary to previous assumptions, the spatial and energetic distribution of the impurity resonance is determined not by the superconducting gap but rather by the pseudogap. Although this interpretation differs from that of previous low temperature STM results (Hudson 2001, Pan 2000), it is consistent with recent experimental and theoretical work.
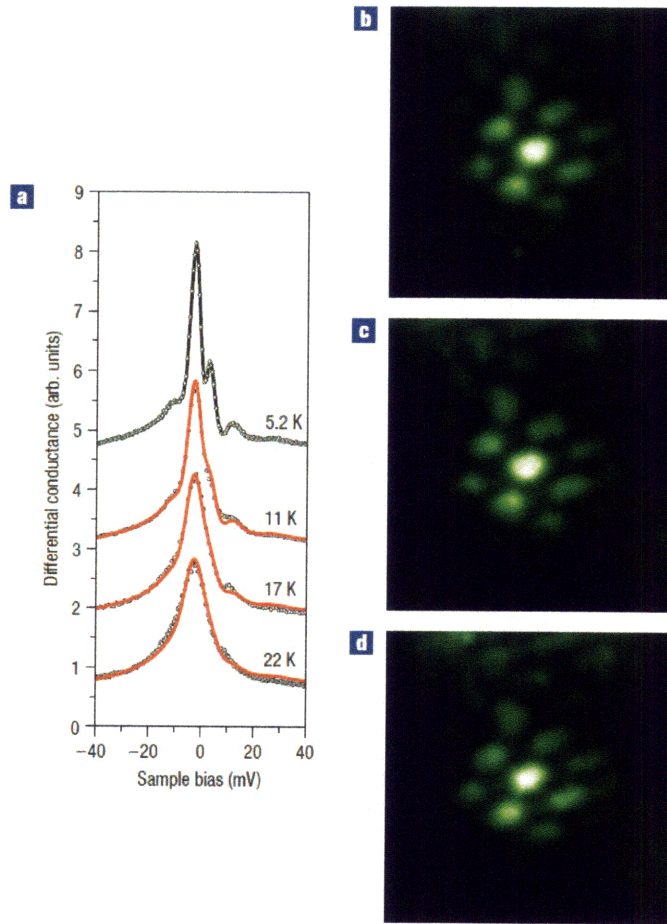
Figure 4.3   Temperature dependence of the impurity resonance through T_C.

a. Evolution of spectra taken at the impurity center, starting from 5.2 K (of Fig. 4.2). For curves at higher temperatures, the experimental data (black circles) are overlaid with red lines, representing the 5.2 K spectrum thermally broadened to the respective temperatures. Even for temperatures above $T_C = 15$ K the match is remarkable.

b-d. The $V_{sample} = -2$ meV conductance maps of the same impurity pictured in Fig. 4.1b (at 5.2 K), tracked as temperature is increased to 11 K (**b**), 17 K (**c**), and 22 K (**d**).

Experimentally, a number of recent results suggest that the pseudogap not only exists above T_C but also coexists with the superconducting gap below T_C (Le Tacon 2006, Tanaka 2006, Boyer 2007, Kondo 2007). Furthermore, NMR measurements have shown that the effects of a staggered paramagnetic polarization induced by Zn in $YBa_2Cu_3O_7$ persist with little temperature dependence from above to below T_C (Ouazi 2006, Ouazi 2004). Ellipsometry experiments have also demonstrated that impurities interact strongly

with the pseudogap (Pimenov 2005), with Zn giving rise to a gradual and inhomogeneous pseudogap suppression while Ni strongly enhances the pseudogap. Both the authors of that work and others (Dora 2007) have interpreted this as evidence of the importance of magnetic correlations in the pseudogap state. Tallon et al. have also stressed the importance of the pseudogap in interpreting the effects of impurities (Tallon 1998, 1997).

Theoretically, several works have discussed the possibility of impurity resonances in the pseudogap state. Kruis et al, for example, argue that neither phase coherence nor a particular gap shape is needed in order to generate a resonance peak near Fermi energy. Instead, any depletion of the density of states at the Fermi energy is sufficient to produce resonance-like bound states near a nonmagnetic impurity (Kruis 2001). Others have independently arrived at a similar conclusion (Zhu 2001, Morr 2002, Wang 2002). Several of these works (Kruis 2001, Zhu 2001, Morr 2002, Wang 2002) even suggest the use of impurity resonances to learn about the nature of the pseudogap, in particular by differentiating between two different pseudogap scenarios – the 'phase fluctuation' and the 'normal state ordering' scenario. Although both of these are rather general labels that encompass a variety of different theories, roughly speaking in the former the pseudogap state arises with warming as the superconducting state is destroyed by phase fluctuations, while in the latter the pseudogap is one of a number of competing orders, prototypically d-density wave (DDW) order (Chakravarty 2001).

Experimentally distinguishing between these two classes of pseudogap has proven difficult, but impurity studies may provide new insights. Wang et al. (Wang 2002) focus on the behavior of the main impurity peak, which they argue would be abruptly broadened slightly above the transition temperature in 'phase fluctuation scenarios,' while in normal state ordering scenarios the impurity peak should remain sharp aside from thermal broadening. Following this result, our data, showing no significant temperature dependence above T_C, point toward a normal state ordering scenario.

Kruis et al. (Kruis 2001) instead focus on the "satellite peak," a feature observable in the central and 2NN spectra of Fig. 4.2 opposite the main peak ($\Omega^{Sat} = -\Omega = 2.75$ meV). This

52

peak has been interpreted as arising from particle-hole symmetry of Bogoliubov quasiparticles in a superconductor (Balatsky 2006, Kruis 2001), in which case its existence should be interpreted as a marker for the local presence of superconductivity. Thus this peak should exist above T_C in the presence of phase fluctuations but not in the case of some other order. Unfortunately this is a difficult test as thermal broadening quickly causes the satellite to merge with the central peak and we cannot from our data distinguish between the disappearance or simple broadening of the satellite. Further experimental studies on weaker impurities which generate higher energy states, such as Ni, should allow for investigation of this proposal.

4.3 Gap in nearest neighbor atoms and concluding discussion

The clear presence of a satellite peak below T_C does however point towards the coexistence of superconductivity and the impurity resonance, as was previously observed near Ni atoms (Hudson 2001). Another marker for superconductivity can be observed in the spectra (Fig. 4.2, 4.4b) taken over the nearest neighbor atoms (the intermediate dark regions in Fig. 4.1b). Here a notable difference exists between spectra taken below T_C (at 5.2 K) and those taken above (at 17 K and 22 K) not captured by simple thermal broadening (Fig. 4.4b). In order to clarify the nature of this change we divide the lower temperature spectra by those taken at exactly the same location at a normalization temperature T_N above T_C (here $T_N = 22$ K). What remains (Fig. 4.4c, blue) is a small gap with half peak to peak separation $\Delta = 5.5$ meV, slightly smaller than the average $\Delta = 6.7 \pm 1.6$ meV we recently reported from similarly normalized spectra taken away from impurities in indistinguishable samples (Boyer 2007). In that work we interpreted this gap, which is homogeneous and vanishes at T_C, as the superconducting gap. Its existence here in the heart of the impurity resonance (on the NN atoms) is consistent with the observation of the satellite peak on the center and 2NN atoms, and indicative of the coexistence of superconductivity and the resonance. That both the asymmetry of the main and satellite peaks and the reduction of the gap size Δ are consistent with a suppression of superconductivity is fascinating.
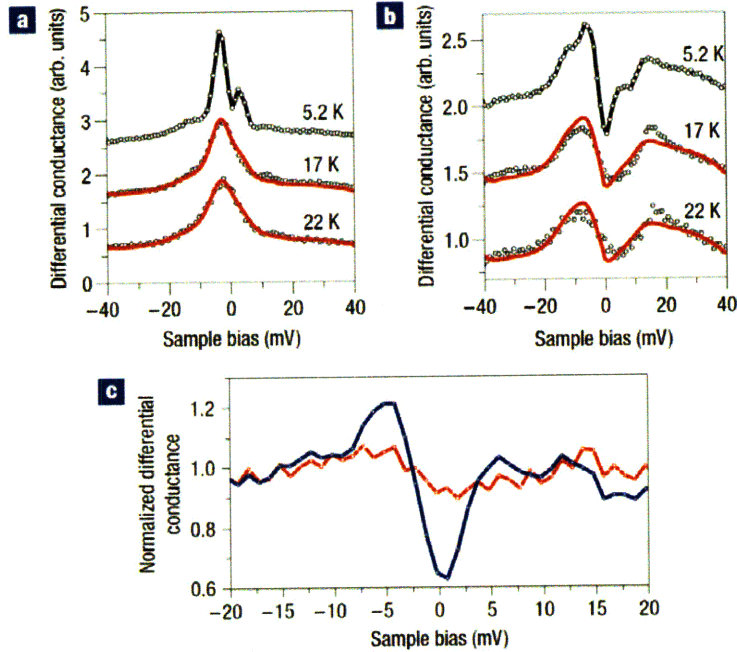
Figure 4.4   Temperature dependence of off-center spectra through T_C.

a. Similar to spectra from the impurity center (Fig. 4.3a), spectra from 2NN regions (black circles) show low energy resonance peaks which are well matched by thermally broadened low temperature data (red lines).

b. In contrast, spectra from the NN Cu atoms (black circles) show instead a gap which is not well matched by the thermally broadened 5.2 K spectrum (red lines) above $T_C = 15$ K.

c. The normalized 5.2 K spectrum of **b** ($T_N = 22$ K) (blue) reveals a small gap not found in the normalized 17 K spectrum (red), consistent with this gap being the superconducting gap.

These results thus point towards an interesting interplay of the pseudogap and superconductivity in determining the nature of impurity resonances in high temperature superconductors. The energetic and spatial distributions of the main resonance appear to be set by the pseudogap, as they show no appreciable temperature dependence (save thermal broadening). On the other hand, the appearance and strength of the satellite peak and the size of the superconducting gap in the non-peaked (nearest neighbor) regions may be indicative of what remains of the superconducting state in the vicinity of the impurity. Continued research, particularly in samples intentionally doped with Zn or Ni, may further disentangle these effects and thus realize the potential of impurity studies to probe the nature of both superconductivity and the pseudogap in these complex materials.

54

Chapter 5

Spatial and doping dependence of impurity resonances

In the last chapter I focused on the temperature dependence of impurity resonance. Impurity resonances are caused by the interaction of impurities with the pseudogap. In this chapter I discuss the doping and spatial dependence of impurity resonance. We have studied the doping dependence of native impurity resonances in Bi-2201, for UD 25 K, OPT 32 K, OPT 35 K and OD 15 K as well as Eu-doped UD 14 K. As doping is increased from underdoped to overdoped the impurity resonance energy moves from positive to negative. Implications of this energy shift with doping for theories of the pseudogap are outlined.

The next section of this chapter illustrates the detailed spatial dependence of the magnitude of the resonance peak around the impurity center. It has long been debated whether the impurity resonance peaks are commensurate with the lattice or appear as the result of scattering and hence can take incommensurate values. We find that the impurity resonance peaks are commensurate with the underlying lattice and that the spatial pattern is similar to that of single slit interference.

Finally, in Bi-2212 it has been observed that impurity resonances are observed only in regions with low gap width. I report the same in Bi-2201 as well. If indeed impurities locally reduce the pseudogap it would be very interesting for evaluation of different theories, however, we discuss other possible hypotheses and the necessity for further work.

5.1   Doping dependence

In the last chapter, the impurity resonance peaks for native impurities in 15 K overdoped samples are found to be at -2.75 mV. In this section we present similar impurity resonances for UD 14 K (Eu-doped), UD 25 K and OPT 35 K samples. Just like the sample discussed in last chapter these samples are not doped with known impurities, so the resonances are due to "native impurities," possibly vacancies. Spatially, the layer corresponding to the peak resonance energy in the differential conductance map is similar to the 15 K overdoped samples discussed in the last chapter. Similar to the OD 15 K sample, the impurity does not affect the topographic layer and the impurity position is not detectable just from the topography. The impurity resonance spectra are also similar to the overdoped sample studied before. Figure 5.1 shows the spectra taken at the center of impurity resonances in Eu-doped underdoped 14 K, UD 25 K and optimally 35 K as well as in OD 15 K sample discussed before.
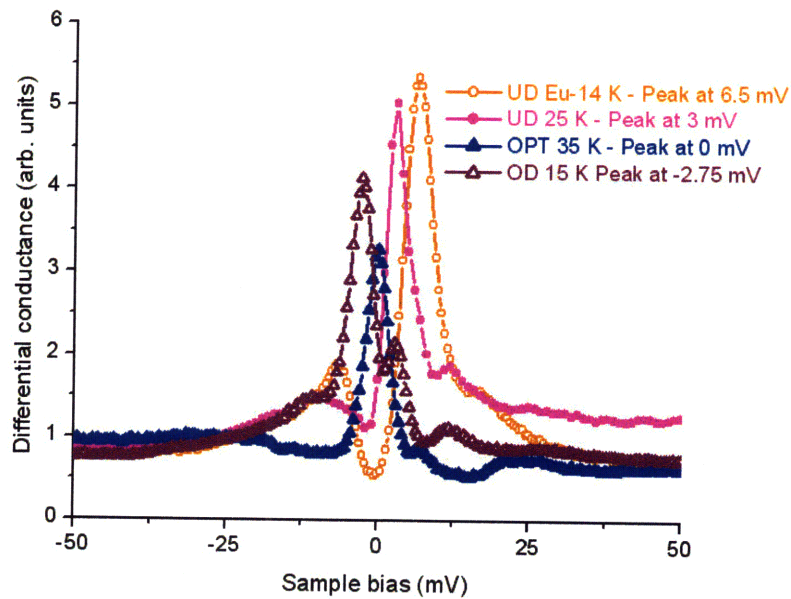

Figure 5.1   Resonance peak at the impurity center for the following samples; Eu-doped underdoped 14 K, UD 25 K, OPT 35 K and OD 15 K. EU doping is not the impurity under consideration; the impurities are native impurity or a vacancy. Energies are indicated in appropriate color codes.

The doping dependence of the resonance peak energies in these three samples is summarized in the following table. As the doping is increased the resonance peak moves from positive energy to negative energy; for optimally doped samples the resonance is at zero energy.

Sample	Resonance peak
Eu-14K UD	6.5 mV
25K UD	3 mV
35K OPD	0 mV
32K OPD	0 mV
15K OD	-2.75 mV

5.2 Implications of the observed doping dependence

In the last chapter we discussed a broad classification of theories of the pseudogap into two groups - the 'phase fluctuation' and the 'normal-state ordering' scenarios. It is predicted (Wang 2002) that in the phase fluctuation case the resonance peak energy is not sensitive to doping. This prediction is at odds with our experimental results, which clearly show a doping dependence for the energy of impurity resonances. Furthermore, in optimally doped samples the peak resonance energy is at zero, while in the calculations of Kruis (2001) and Wang (2002) the resonant energy always appears as proportional to the pseudogap energy scale. However, Zhu *et. al.* (Zhu 2001) have studied the electronic structure around a single nonmagnetic impurity in the d-density wave (DDW) ordering. Just like the case of pure superconducting state, this interaction with DDW leads to a subgap resonance peak, and they found conditions under which the peak could be exactly at zero. They also concluded that for the DDW model of the pseudogap the resonance peak in the conductance near a unitary nonmagnetic impurity would have a strong doping dependence.

Although our measured doping dependence lends strong support to a model such as Zhu et al, clearly more work needs to be done both experimentally and theoretically. In the former, we are most concerned that our measurements were made on "native" (unintentionally doped) impurities. They could, for example, even be different elements in the different samples. That the observed monotonic doping dependence could be a result of coincidence seems unlikely, however, further study on intentionally doped samples, for example those doped with Zn or other non magnetic impurities, would put this concern to rest. On the theoretical side, that our doping dependence agrees with predictions from one DDW model cannot be considered proof of the model, but rather indicates that some feature of the model captures the correct behavior. It would be useful to see how general this feature is and whether we can actually confirm or exclude an entire scenario, such as the 'phase fluctuation scenario,' rather than just individual models within it.

5.3 Spatial dependence of the impurity resonance

In addition to doping dependence, we have also made careful measurements of the spatial dependence of impurity resonances. The top panel of Fig. 5.2 is a reproduction of Fig. 4.1b, showing a $V_{sample} = -2$ meV differential conductance map in OD 15 K Bi-2201 sample. The spatial distribution of the impurity resonance has d-wave symmetry as has been previously reported for Bi-2212 (Hudson 2001, Pan 2000). The much talked about "cross shape" in the LDOS map appears because the nearest neighbor copper sites do not show an impurity resonance signal. This results in a 45 degree angle between the topography and the spectral map major axis. There have been several theoretical attempts to explain this distribution, among which are Salkola (1996) and Tang (2004), who modeled non-magnetic impurities as scalar potentials. According to theory, for strong point like scalar potentials the spectral weight of the resonance should be zero at the impurity center. This is in clear opposition to the experiments. Martin (2002) attempted to explain experimental results by using an asymmetrical tunneling filter between the CuO_2 and BiO layer. The most comprehensive explanation was provided by Tang (2004) who instead of a point like potential took a potential that extended over nearest neighbor (NN). Additionally, they included a modification of the pairing potential and the hopping

energies in the neighborhood of the Zn site and modeled a resonance in agreement with the experiments.

The theoretical calculations mentioned above are based on how a superconducting gap would interact with the impurity. In the light of new development that resonances appear due to interactions with the pseudogap we turn to calculations based on interactions with the pseudogap. Wang (2002) presented calculations based on a DDW model of the pseudogap, which highlight significant differences in spatial distribution from experimental observations. It is predicted, for example, that the impurity resonance shall not peak at the impurity center but instead on the nearest neighbor Cu atoms. Although the origin of this discrepancy remains unknown, it may be in the treatment of the impurity as a point like scalar potential.

Although the "cross shape" and the observed signal at the impurity center were separately explained by both Martin (2002) and Tang (2002, 2004) there are major differences in their approach. According to Martin (2002) there is no reason for impurity resonance peaks to be commensurate with the lattice; though the impurity is located at a lattice point, the location of subsequent peaks are determined by the interference of scattered waves with the Fermi wavevector. Experimentally, it was observed that the subsequent peaks are close to the lattice points but not on top of them. In the analysis done by Tang (2004) the grid was taken to be the same as the lattice grid forcing the resonances to be commensurate. The resolution of the previous impurity data on Bi-2212 was not adequate to resolve this question. Here we report spectral maps with much higher spatial resolution that enables us to confirm that impurity resonances are indeed commensurate with the lattice.

First of all, close observation of conductance maps imaged at the impurity peak energy and simultaneously acquired topography shows that while the main impurity peak is on top of a lattice point, subsequent peaks appear to be displaced slightly toward the impurity center. In the differential conductance map of Fig. 5.2 we take two line cuts along lines at 45 degrees to each other, indicated in red and green. We show the impurity

resonance intensity as a function of position along these lines (where x = 0 is set to the resonance center). The intensity, $I(x)$ is fit nicely by an exponential decaying periodic pattern

$$I(x) = A e^{-\frac{1}{(2\omega)^2}x^2} \left(\cos^2 (\pi x / \lambda) + I_0 \right) \tag{5.1}$$

Importantly, the exponentially decaying envelope can lead to mistaken estimates of the modulation wavelength. For example, along the lattice direction (red) the wavelength appears to be about 1.8 a_0, yet the fit reveals $\lambda = 2.07(2)$ a_0. Similarly, along the diagonal (green), the wavelength is not the 1.25 a_0 it appears to be, but rather 1.42(2) a_0, confirming that the pattern is commensurate with the atomic lattice.
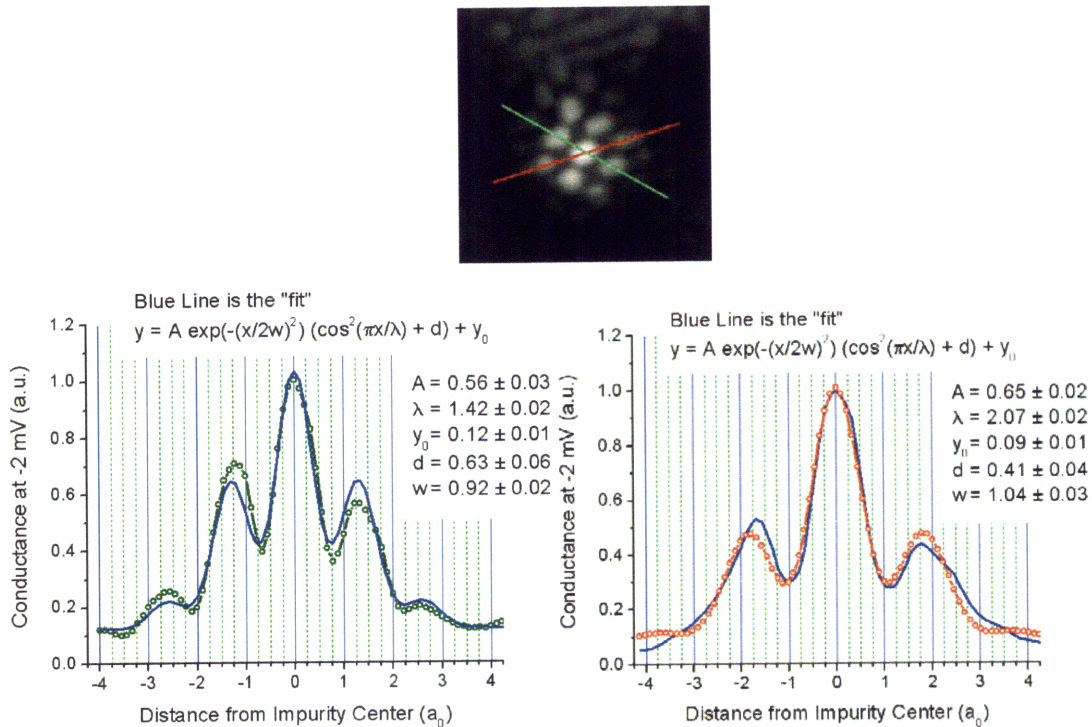

Figure 5.2   Fitting the resonance signal. Top panel – the conductance map corresponding to -2 mV layer. The directions of line cuts; the red and green line are indicated. Bottom panels – actual intensity (circles) and the fit (blue lines) for each direction. The x axis scale is in terms of the lattice spacing. The fitting parameters are in inset.

We can model the entire conductance map by combining the 1D curve fits into a 2D fit.

$$I(x, y) = A e^{-\frac{1}{(2\omega)^2}\left(x^2 + y^2\right)} \left(\cos^2\left(\frac{\pi}{\lambda} x\right) \cos^2\left(\frac{\pi}{\lambda} y\right) + I_0 \right) \qquad (5.2)$$

Fitting with this form we find $\lambda = 1.41\ a_0$, as is expected for a pattern which is rotated 45°
to the lattice and omits the nearest neighbor atoms. The exponential decay is so strong
that the signal disappears beyond the eight points surrounding the center peak.
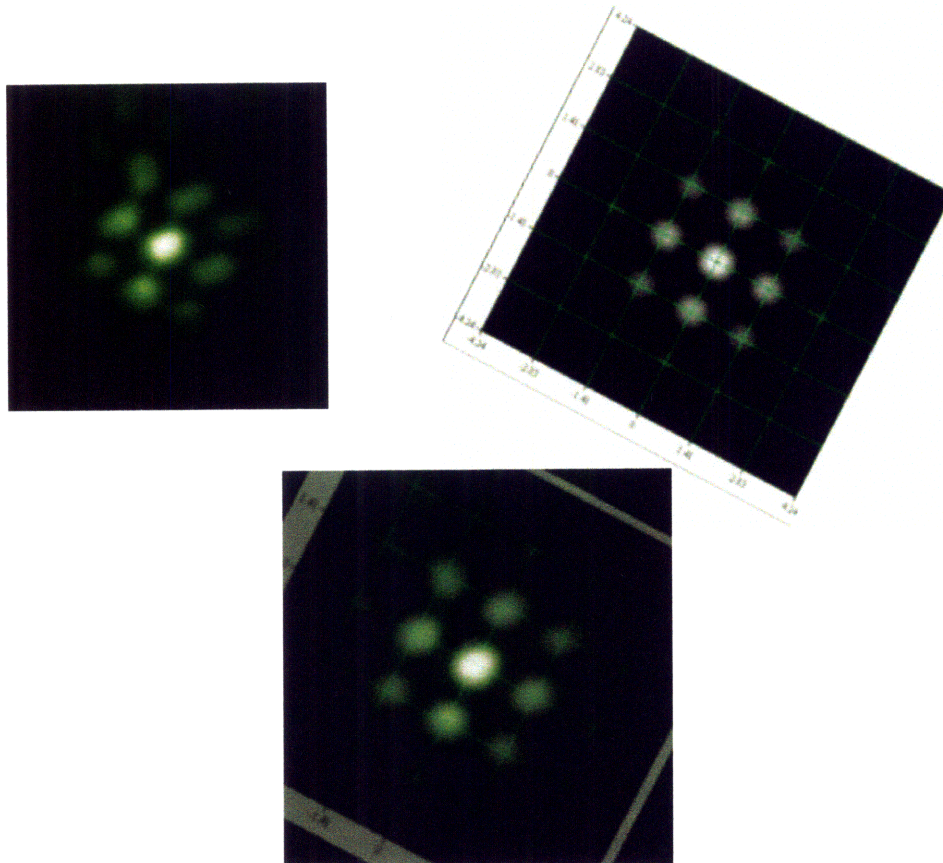

Figure 5.3   The interference pattern and actual impurity resonance. Top right panel is a plot
               of the interference pattern on a grid 1.41 times the atomic lattice. Without any
               exponential decay the grid points are where impurity resonances should be.
               Bottom panel –impurity resonance signal and the interference pattern are
               superimposed.

In Fig. 5.3 we plot the theoretical interference pattern (top right). The green grid lines run through the subset of the atomic lattice on which the impurity resonance peaks lie. In the bottom panel we overlap the experimental and calculated results.

5.4   Impurity location and pseudogap width

It has been reported in the literature that impurity resonances are visible only in parts of the sample where the gap in the density states is low (Lang 2002). In Bi-2212 it is hard to distinguish whether this statement applies to the superconducting gap or the pseudogap. None-the-less, when compared to the inhomogeneous distribution of the STM-measured gap, Lang *et al.* (2002) reported that impurity resonances appear only where the nearby gap is in lower half of the distribution (less than about 50 meV). They went on to estimate that given the large field of view in the data and the number of impurities observed, the probability that the observed correlation is a result of mere coincidence is statistically insignificant.

We report similar observations in our studies of Bi-2201 across multiple dopings. For three different samples we observe a similar correlation – impurity resonances are located only in areas of low gap.

There are three important hypotheses for this effect

a) The impurity resonance is observable by virtue of the local gap being low.

b) During the growth process, impurities are attracted to lower gap areas. Lower gap areas might be a result of local differences in oxygen doping resulting in local strain differences, which could reasonably explain this effect.

c) The impurities reduce the local gap – an interesting hypothesis which might explain why impurities reduce the transition temperature (and hence the associated energy gap) in the bulk. This hypothesis, if true, might help differentiate theories of the pseudogap and superconducting gap.

62

In an effort to observe the change of pseudogap width as the impurity center is approached we begin with a spectral survey map at 22 K, above the 15 K transition temperature for the sample. At this temperature we assume that the observed gap is only the pseudogap. With our high resolution data it is possible to observe a gradual reduction of the gap while approaching impurity center, for example in the waterfall plot of Fig. 5.4.
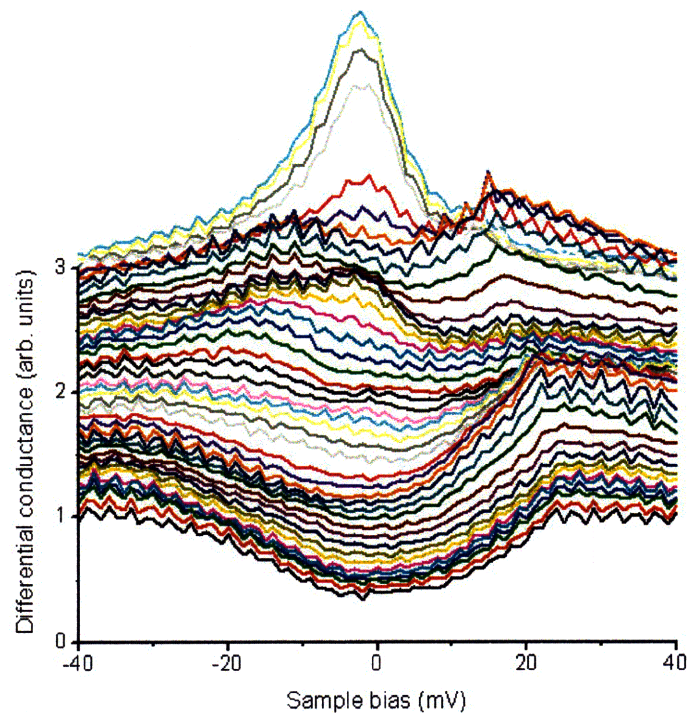

Figure 5.4   Spectra extracted along the red line of Fig. 5.2 from four lattice constants away (bottom) towards the impurity center (top). Data taken on the OD 15 K sample of chapter 4 at 22 K.

Unfortunately, this result alone cannot differentiate the hypotheses discussed above, and other experimental measurements, perhaps using surface impurities which can be moved from small gap into large gap regions, will be needed to determine the explanation of this interesting observation.

5.5 Outlook and further research

Doping dependence of the impurity resonance energy with known doping

As seen in section 5.1, the doping dependence of native impurities show a clear pattern of resonance peak energies moving from positive values in underdoped samples to negative value in overdoped samples. The resonant peak is at zero bias for the optimally doped samples. This result could be used for evaluating different theories of pseudogap, but first needs confirmation with a known non-magnetic impurity like Zn.

Temperature dependence of the satellite peak

In chapter 4 we learned in detail about the temperature dependence of the resonance peak produced by impurities. Similarly, temperature dependence of the satellite peak is expected to provide a wealth of information. In the sample studied (OD 15 K) the temperature dependence of the satellite peak for these native impurities is obscured by closeness of satellite peak to the mean peak. For impurity atoms with peaks further apart the temperature dependence of the satellite peak will be observable. Ni being a weaker impurity, and hence expected to have resonance further away from Fermi energy, as observed in Bi-2212 (Hudson 2001) we suggest the study of samples with Ni doping.

In the results of Hudson (Hudson 2001 Figure 4) Fig. 2a shows the -9 mV layer corresponding to the main peak, and Fig. 2b shows the + 9 mV layer corresponding to the satellite peak. Spatially, the positive and negative bias patterns are different and complimentary. The satellite peak appears due to the symmetry of Bogoliubov quasiparticles and is an indication of superconductivity. It is expected that above T_C the main peak would survive and the complimentary pattern at negative bias due to the satellite peak would disappear. Many in the community are eager to confirm this result. This experiment would require a 2201 sample with relatively low T_C (preferably below 25 K), both because higher temperatures entail more thermal broadening and because the main resonance peak and satellite peak need to be well separated in energy and as we have reported here, near optimal doping, the resonance, and hence satellite, are close to the Fermi energy.

Contrast results of Ni-and Zn dopants

In previous studies of Bi-2212 the results from samples with Ni and Zn doping were compared, revealing important differences in the effects of magnetic and non-magnetic impurities (Hudson 2001). Similarly, such studies in Bi-2201, most likely using Ni and Zn dopants, could yield important results. For example, the superconducting gap and pseudo gap are expected to behave differently around magnetic and non magnetic impurities. This could solidify our understanding of the two gaps we have observed in this system (Boyer 2007). It may even shine light on the origin of interactions in the phase transition from pseudogap to superconducting phase.

Relate pseudogap inhomogeneity and impurity resonance location

As described in section 5.3 of this chapter, impurity resonances appear only in regions where pseudogap width is low. This relationship is established, but its interpretation and a full understanding of its consequences require more tests and advances in theoretical understanding.

Studies of impurity resonance above T*

In the last chapter we established the relationship between pseudogap and impurity resonance. It is known that the pseudogap phase persists up to temperature T*. The impurity resonance is expected to disappear as the sample is warmed above T*. In many samples T* is very high ~150 K – 250 K, so it is hard to detect any impurity resonance peak due to thermal broadening. To successfully observe the disappearance of impurity resonance the samples need to have low T*. For example overdoped Bi-2201 with T_C below 15 K is expected to have T* of the order of 80 - 110 K. If the impurity resonance remains as strong as we have observed in our overdoped 15 K samples then it would be detectable even at around 100 K. We theoretically broadened the spectrum (of our 15 K sample) to above 100 K and the resonance peak and spatial impurity resonance pattern is still detectable. So it should be possible to observe the disappearance of impurity resonances for transitions through T*. Highly overdoped Bi-2201 samples with lower T_C (10 ~ 15 K) are good candidates for this study.

Bibliography

Agrait, N., "Vertical inertial piezoelectric translation device for a scanning tunneling microscope." *Rev. Sci. Inst.* **63**, 263 (1992).

Alloul, H., Bobroff, J., Gabay, M., and Hirschfeld, P.J., "Defects in correlated metals and superconductors." *Rev. Mod. Phys.* **81**, 45 (2009).

Anderson, P.W., "New Approach to the Theory of Superexchange Interactions." *Phys. Rev.* **115**, 2 (1959).

Balatsky, A.V., Vekhter, I., and Zhu, J.-X., "Impurity-induced states in conventional and unconventional superconductors." *Rev. Mod. Phys.* **78**, 373 (2006).

Bardeen, J., Cooper, L.N., and Schrieffer, J.R., "Microscopic Theory of Superconductivity." *Phys. Rev.* **106**, 162 (1957a).

Bardeen, J., Cooper, L.N., and Schrieffer, J.R., "Theory of Superconductivity." *Phys. Rev.* **108**, 1175 (1957b).

Bardeen, J., "Tunneling from a Many-Particle Point of View." *Phys. Rev. Lett.* **6**, 57 (1961).

Barrett, S.E., *et al.*, "Cu63 Knight shifts in the superconducting state of $YBa_2Cu_3O_{7-d}$ (Tc=90 K)." *Phys. Rev. B* **41**, 6283 (1990).

Basov, D.N. and Timusk, T., "Electrodynamics of high- Tc superconductors." *Rev. Mod. Phys.* **77**, 721 (2005).

Batlogg, B., *et al.*, "Normal state phase diagram of $(La,Sr)_2CuO_4$ from charge and spin dynamics." *Physica C* **235-240**, 130 (1994).

Bednorz, J.G. and Müller, K.A., "Possible high Tc superconductivity in the Ba−La−Cu−O system." *Z. Phys. B* **64**, 189 (1986).

Binnig, G. and Rohrer, H., "Scanning Tunneling Microscopy." *Helv. Phys. Acta* **55**, 726 (1982a).

Binnig, G., Rohrer, H., Gerber, C., and Weibel, E., "Surface Studies by Scanning Tunneling Microscopy." *Phys. Rev. Lett.* **49**, 57 (1982b).

Blackford, B.L. and Jericho, M.H., "A hammer-action micropositioner for scanning probe microscopes." *Rev. Sci. Inst.* **68**, 133 (1997).

Bobroff, J., *et al.*, "Persistence of Li Induced Kondo Moments in the Superconducting State of Cuprates." *Phys. Rev. Lett.* **86**, 4116 (2001).

Bonn, D.A., Dosanjh, P., Liang, R., and Hardy, W.N., "Evidence for rapid suppression of quasiparticle scattering below Tc in $YBa_2Cu_3O_{7-delta}$." *Phys. Rev. Lett.* **68**, 2390 (1992).

Bonn, D.A., *et al.*, "A limit on spin-charge separation in high-Tc superconductors from the absence of a vortex-memory effect." *Nature* **414**, 887 (2001).

Boyer, M.C., *et al.*, "Imaging the two gaps of the high-temperature superconductor $Bi_2Sr_2CuO_{6+x}$." *Nature Phys.* **3**, 802 (2007).

Chakravarty, S., Laughlin, R.B., Morr, D.K., and Nayak, C., "Hidden order in the cuprates." *Phys. Rev. B* **63**, 094503 (2001).

Chatterjee, K., *et al.*, "Visualization of the interplay between high-temperature superconductivity, the pseudogap and impurity resonances." *Nature Phys.* **4**, 108 (2008).

Chen, C.J., Introduction to Scanning Tunneling Microscopy 1993, Oxford: Oxford University Press.

Chen, X., Frank, E.R., and Hamers, R.J., "An atomic-resolution cryogenic scanning tunneling microscope." *Rev. Sci. Inst.* **65**, 3373 (1994).

Colclough, M.S., "A fast high-voltage amplifier for driving piezoelectric positioners." *Rev. Sci. Inst.* **71**, 4323 (2000).

Cooper, L.N., "Bound Electron Pairs in a Degenerate Fermi Gas." *Phys. Rev.* **104**, 1189 (1956).

Damascelli, A., Hussain, Z., and Shen, Z.-X., "Angle-resolved photoemission studies of the cuprate superconductors." *Rev. Mod. Phys.* **75**, 473 (2003).

Demuth, J.E., Hamers, R.J., Tromp, R.M., and Welland, M.E., "A simplified scanning tunneling microscope for surface science studies." *JVST A* **4**, 1320 (1986).

Dora, B., Maki, K., Virosztek, A., and Vanyolos, A., "Pseudogap enhancement due to magnetic impurities in d-density waves." *Phys. Rev. B* **75**, 132504 (2007).

Fauque, B., *et al.*, "Magnetic Order in the Pseudogap Phase of High-T_C Superconductors." *Phys. Rev. Lett.* **96**, 197001 (2006).

Fein, A.P., Kirtley, J.R., and Feenstra, R.M., "Scanning tunneling microscope for low temperature, high magnetic field, and spatially resolved spectroscopy." *Rev. Sci. Inst.* **58**, 1806 (1987).

Fischer, Ø., *et al.*, "Scanning tunneling spectroscopy of high-temperature superconductors." *Rev. Mod. Phys.* **79**, 353 (2007).

Frohn, J., Wolf, J.F., Besocke, K., and Teske, M., "Coarse tip distance adjustment and positioner for a scanning tunneling microscope." *Rev. Sci. Inst.* **60**, 1200 (1989).

Gammel, P.L., *et al.*, "Observation of Hexagonally Correlated Flux Quanta In $YBa_2Cu_3O_7$." *Phys. Rev. Lett.* **59**, 2592 (1987).

Gough, C.E., *et al.*, "Flux quantization in a high-Tc superconductor." *Nature* **326**, 855 (1987).

Grosso, G. and Parravicini, G., Solid State Physics. 2000: Academic Press.

Guha, A., Kim, S., and de Lozanne, A.L., "Novel frictionless approach mechanism for a scanning tunneling microscope." *Rev. Sci. Inst.* **74**, 4384 (2003).

Gupta, A.K. and Ng, K.W., "Compact coarse approach mechanism for scanning tunneling microscope." *Rev. Sci. Inst.* **72**, 3552 (2001).

Hardy, W.N., *et al.*, "Precision measurements of the temperature dependence of lambda in YBa2Cu3O6.95: Strong evidence for nodes in the gap function." *Phys. Rev. Lett.* **70**, 3999 (1993).

Hudson, E. W. (1999). Investigating High-TC Superconductivity on the Atomic Scale by Scanning Tunneling Microscopy. Physics. Berkeley, University of California at Berkeley. **PhD:** 99.

Hudson, E.W., *et al.*, "Interplay of magnetism and high-T_c superconductivity at individual Ni impurity atoms in $Bi_2Sr_2CaCu_2O_{8+\delta}$." *Nature* **411**, 920 (2001).

Hudson, E.W., *et al.*, "STM study of novel resonances in $Bi_2Sr_2CaCu_2O_{8+\delta}$." *Physica B* **329-333**, 1365 (2003).

Imada, M., Fujimori, A., and Tokura, Y., "Metal-insulator transitions." *Rev. Mod. Phys.* **70**, 1039 (1998).

Kalthoff. T et. al. 1991, http://focus.ti.com/lit/an/sboa002/sboa002.pdf

Kamihara, Y., Watanabe, T., Hirano, M., and Hosono, H., "Iron-Based Layered Superconductor $La[O_{1-x}F_x]FeAs$ (x = 0.05-0.12) with Tc = 26 K." *J. Am. Chem. Soc.* **130**, 3296 (2008).

Kaminski, A., *et al.*, "Quasiparticles in the Superconducting State of $Bi_2Sr_2CaCu_2O_{8+\delta}$." *Phys. Rev. Lett.* **84**, 1788 (2000).

Kluge, T., *et al.*, "Clear distinction between the underdoped and overdoped regime in the T_c suppression of Cu-site-substituted high-T_c cuprates." *Phys. Rev. B* **52**, R727 (1995).

Kondo, T., *et al.*, "Contribution of electronic structure to thermoelectric power in $(Bi,Pb)_2(Sr,La)_2Cu\ O_{6+\delta}$." *Phys. Rev. B* **72**, 024533 (2005).

Kondo, T., *et al.*, "Evidence for Two Energy Scales in the Superconducting State of Optimally Doped $(Bi,Pb)_2(Sr,La)_2CuO_{6+\delta}$." *Phys. Rev. Lett.* **98**, 267004 (2007).

Krishana, K., Harris, J.M., and Ong, N.P., "Quasiparticle Mean Free Path in $YBa_2Cu_3O_7$ Measured by the Thermal Hall Conductivity." *Phys. Rev. Lett.* **75**, 3529 (1995).

Kruis, H.V., Martin, I., and Balatsky, A.V., "Impurity-induced resonant state in a pseudogap state of a high-T_c superconductor." *Phys. Rev. B* **64**, 054501 (2001).

Lang, K.M., *et al.*, "Imaging the granular structure of high-T_C superconductivity in underdoped $Bi_2Sr_2CaCu_2O_{8+\delta}$." *Nature* **415**, 412 (2002).

Le Tacon, M., *et al.*, "Two energy scales and two distinct quasiparticle dynamics in the superconducting state of underdoped cuprates." *Nature Phys.* **2**, 537 (2006).

Lee, P.A., Nagaosa, N., and Wen, X.-G., "Doping a Mott insulator: Physics of high-temperature superconductivity." *Rev. Mod. Phys.* **78**, 17 (2006).

MacFarlane, W.A., *et al.*, "Dynamics of the Local Moment Induced by Nonmagnetic Defects in Cuprates." *Phys. Rev. Lett.* **85**, 1108 (2000).

MacLeod, J.M., *et al.*, "Two linear beetle-type scanning tunneling microscopes." *Rev. Sci. Inst.* **74**, 2429 (2003).

Maeda, A., *et al.*, "Substitution of 3d metals for Cu in $Bi_2(Sr_{0.6}Ca_{0.4})_3Cu_2O_y$." *Phys. Rev. B* **41**, 4112 (1990).

Maeda, H., Tanaka, Y., Fukutomi, M., and Asano, T., "A New High-T_c Oxide Superconductor without a Rare Earth Element." *Japanese Journal of Applied Physics* **27**, L209 (1988).

Maeda, H. and Togano, K., eds. *Bismuth-based High-temperature Superconductors*. Applied Physics Series, No 6. 1996, CRC: New York.

Martin, I., Balatsky, A.V., and Zaanen, J., "Impurity States and Interlayer Tunneling in High Temperature Superconductors." *Phys. Rev. Lett.* **88**, 097003 (2002).

Maxwell, E., "Isotope Effect in the Superconductivity of Mercury." *Phys. Rev.* **78**, 477 (1950).

Meissner, W. and Ochsenfeld, R., "Ein neuer Effekt bei Eintritt der Supraleitfähigkeit." *Naturwissenschaften* **21**, 787 (1933).

Morr, D.K., "Resonant Impurity States in the d-Density-Wave Phase." *Phys. Rev. Lett.* **89**, 106401 (2002).

Nachumi, B., *et al.*, "Muon Spin Relaxation Studies of Zn-Substitution Effects in High-T_c Cuprate Superconductors." *Phys. Rev. Lett.* **77**, 5421 (1996).

Niedermayer, C., *et al.*, "Common Phase Diagram for Antiferromagnetism in La2-xSrxCuO4 and Y1-xCaxBa2Cu3O6 as Seen by Muon Spin Rotation." *Phys. Rev. Lett.* **80**, 3843 (1998).

Okada, Y. and Ikuta, H., "R dependence of superconductivity and thermopower in the $Bi_2Sr_{2-x}R_xCuO_y$ (R = La, Sm and Eu) system." *Physica C* **445-448**, 84 (2006).

Onnes, H.K., "Further experiments with liquid helium. C. On the change of electrical resistance of pure metals at very low temperatures, etc. IV. The resistance of pure mercury at helium temperatures." *Comm. Phys. Lab. Univ. Leiden* **120b**, 3 (1911).

Ouazi, S., Bobroff, J., Alloul, H., and MacFarlane, W.A., "Correlation length in cuprate superconductors deduced from impurity-induced magnetization." *Phys. Rev. B* **70**, 104515 (2004).

Ouazi, S., *et al.*, "Impurity-Induced Local Magnetism and Density of States in the Superconducting State of YBa2Cu3O7." *Phys. Rev. Lett.* **96**, 127005 (2006).

Pan, S.H., Hudson, E.W., and Davis, J.C., "^{3}He refrigerator based very low temperature scanning tunneling microscope." *Rev. Sci. Inst.* **70**, 1459 (1999).

Pan, S.H., *et al.*, "Imaging the effects of individual zinc impurity atoms on superconductivity in $Bi_2Sr_2CaCu_2O_{8+\delta}$." *Nature* **403**, 746 (2000).

Pimenov, A.V., *et al.*, "Nickel Impurity-Induced Enhancement of the Pseudogap of Cuprate High-T_c Superconductors." *Phys. Rev. Lett.* **94**, 227003 (2005).

Pohl, D.W., "Dynamic piezoelectric translation devices." *Rev. Sci. Inst.* **58**, 54 (1987).

Puchkov, A.V., Basov, D.N., and Timusk, T., The pseudogap state in high-superconductors: an infrared study. 1996. p. 10049.

Rajagopal, H., *et al.*, "Neutron Structural Studies of Superconducting $Bi_2Sr_2CuO_{-6}$ and $Bi_{2-x}Pb_xSr_{1.8}La_{0.2}Cu_{6+d}$ (x=0.0 and 0.2)." *Japanese Journal of Applied Physics* **32**, 1595 (1993).

Renner, C., Niedermann, P., Kent, A.D., and Fischer, O., "A vertical piezoelectric inertial slider." *Rev. Sci. Inst.* **61**, 965 (1990).

Reynolds, C.A., Serin, B., Wright, W.H., and Nesbitt, L.B., "Superconductivity of Isotopes of Mercury." *Phys. Rev.* **78**, 487 (1950).

Rust, H.P., Buisset, J., Schweizer, E.K., and Cramer, L., "High precision mechanical approach mechanism for a low temperature scanning tunneling microscope." *Rev. Sci. Inst.* **68**, 129 (1997).

Salkola, M.I., Balatsky, A.V., and Scalapino, D.J., "Theory of Scanning Tunneling Microscopy Probe of Impurity States in a D-Wave Superconductor." *Phys. Rev. Lett.* **77**, 1841 (1996).

Shen, Z.X., *et al.*, "Anomalously large gap anisotropy in the a-b plane of $Bi_2Sr_2CaCu_2O_{8+\delta}$." *Phys. Rev. Lett.* **70**, 1553 (1993).

Singh, A. and Ghosh, H., "Stability of the doped antiferromagnetic state of the t-t' Hubbard model." *Phys. Rev. B* **65**, 134414 (2002).

Slezak, J. A. (2007). Atomic-scale impact of unit cell dimensions on pairing in a high-temperature superconductor. Physics. Ithaca, Cornell University. **PhD:** 99.

Sonnenfeld, R., *et al.*, "Semiconductor topography in aqueous environments: Tunneling microscopy of chemomechanically polished (001) GaAs." *App. Phys. Lett.* **50**, 1742 (1987).

Stroscio, J.A., Feenstra, R.M., and Fein, A.P., "Electronic Structure of the Si(111) 2 x 1 Surface by Scanning-Tunneling Microscopy." *Phys. Rev. Lett.* **57**, 2579 (1986).

Subramanian, M.A., *et al.*, A New High-Temperature Superconductor: $Bi_2Sr_{3-x}Ca_xCu_2O_{8+y}$. 1988. p. 1015.

Sun, G.F., *et al.*, "Tc enhancement of $HgBa_2Ca_2Cu_3O_{8+d}$ by Tl substitution." *Physics Letters A* **192**, 122 (1994).

Takeuchi, T., *et al.*, "Topology of the fermi surface and band structure near the fermi level in the Pb-doped Bi2Sr2CuO6+[delta] superconductor." *Journal of Electron Spectroscopy and Related Phenomena* **114-116**, 629 (2001).

Takigawa, M., Hammel, P.C., Heffner, R.H., and Fisk, Z., "Spin susceptibility in superconducting $YBa_2Cu_3O_7$ from Cu^{63} Knight shift." *Phys. Rev. B* **39**, 7371 (1989).

Tallon, J.L., Bernhard, C., Williams, G.V.M., and Loram, J.W., "Zn-induced T_c Reduction in High-T_c Superconductors: Scattering in the Presence of a Pseudogap." *Phys. Rev. Lett.* **79**, 5294 (1997a).

Tallon, J.L., Williams, G.V.M., Flower, N.E., and Bernhard, C., "Phase separation, pseudogap and impurity scattering in the HTS cuprates." *Physica C* **282-287**, 236 (1997b).

Tallon, J.L., "Normal-state pseudogap in $Bi_2Sr_2CaCu_2O_8$ characterized by impurity scattering." *Phys. Rev. B* **58**, R5956 (1998).

Tanaka, K., *et al.*, "Distinct Fermi-Momentum-Dependent Energy Gaps in Deeply Underdoped Bi2212." *Science* **314**, 1910 (2006).

Tang, J.-M. and Flatté, M.E., "Van Hove features in $Bi_2Sr_2CaCu_2O_{8+\delta}$ and effective parameters for Ni impurities inferred from STM spectra." *Phys. Rev. B* **66**, 060504 (2002).

Tang, J.-M. and Flatté, M.E., "Impurity-induced low-energy resonances in $Bi_2Sr_2CaCu_2O_{8+\delta}$." *Phys. Rev. B* **70**, 140510 (2004).

Tersoff, J. and Hamann, D.R., "Theory and Application for the Scanning Tunneling Microscope." *Phys. Rev. Lett.* **50**, 1998 (1983).

Tersoff, J. and Hamann, D.R., "Theory of the scanning tunneling microscope." *Phys. Rev. B* **31**, 805 (1985).

Timusk, T. and Statt, B., "The pseudogap in high-temperature superconductors: an experimental survey." *Rep. Prog. Phys.* **62**, 61 (1999).

Tsuei, C.C., *et al.*, "Pairing Symmetry and Flux Quantization in a Tricrystal Superconducting Ring of YBa2Cu3O7- delta." *Phys. Rev. Lett.* **73**, 593 (1994).

Wang, Q.-H., "Mechanism of Pseudogap Probed by a Local Impurity." *Phys. Rev. Lett.* **88**, 057002 (2002).

Williams, G.V.M., Tallon, J.L., and Dupree, R., "NMR study of magnetic and nonmagnetic impurities in $YBa_2Cu_4O_8$." *Phys. Rev. B* **61**, 4319 (2000).

Wu, M.K., *et al.*, "Superconductivity at 93 K in a new mixed-phase Yb-Ba-Cu-O compound system at ambient pressure." *Phys. Rev. Lett.* **58**, 908 (1987).

Wynn, J.C., *et al.*, "Limits on Spin-Charge Separation from h/2e Fluxoids in Very Underdoped $YBa_2Cu_3O_{6+x}$." *Phys. Rev. Lett.* **87**, 197002 (2001).

Xia, J., *et al.*, "Polar Kerr-Effect Measurements of the High-Temperature $YBa_2Cu_3O_{6+x}$ Superconductor: Evidence for Broken Symmetry near the Pseudogap Temperature." *Phys. Rev. Lett.* **100**, 127002 (2008).

Yazdani, A., *et al.*, "Impurity-Induced Bound Excitations on the Surface of $Bi_2Sr_2CaCu_2O_8$." *Phys. Rev. Lett.* **83**, 176 (1999).

Zhang, F.C. and Rice, T.M., "Effective Hamiltonian for the superconducting Cu oxides." *Phys. Rev. B* **37**, 3759 (1988).

Zhu, J.-X., Kim, W., Ting, C.S., and Carbotte, J.P., "Quasiparticle States around a Nonmagnetic Impurity in a d-Density-Wave State of High-T_c Cuprates." *Phys. Rev. Lett.* **87**, 197001 (2001).